國立臺灣大學理學院地質科學研究所

碩士論文

Department of Geosciences
College of Science
National Taiwan University
Master Thesis

台灣東北部地區高山湖泊的演化過程與沉積作用之探討，以三星妹池為例

Succession and sedimentation process in a small mountainous lake in NE Taiwan: the study of Sanxingmei Pond

許冠毅

Kuan-Yi Hsu

指導教授：施路易 博士

Advisor: Ludvig Löwemark Ph.D.

中華民國 112 年 10 月

October 2023

doi:10.6342/NTU202304291

致謝

I want to sincerely thank my advisor, Professor Ludvig Löwemark, for his guidance over these three years. He never once dismissed my ideas and consistently provided valuable feedback, enabling me to learn and gain insights even when I ventured down the wrong path. In the first year of my graduate studies, we had planned to travel to Thailand to analyze the Asian climate system. Unfortunately, the outbreak of Covid disrupted all our plans. However, Ludvig continued encouraging and steered me back onto the right track. He never blamed me despite potential delays in the research process due to various factors. Instead, he encouraged me to learn from these experiences and consistently reminded me to allocate my limited time wisely.

I wish to thank Professor George Burr for being the chair of my oral defense and for meticulously reviewing and editing my thesis. Professor Burr always wore a warm smile and patiently addressed all my queries. He could guide me step by step, starting from the most fundamental theories, to find the answers I sought. As the chair of my oral defense, Professor Burr dedicatedly corrected every word and sentence, teaching me the most orthodox structure for academic paper writing. I am immensely grateful for his dedicated guidance.

I also want to thank Professor André Bahr and Dr. Stefanie Kaboth-Bahr, who served as members of my oral examination committee and traveled from Germany to Taiwan to participate in my defense. André and Stefanie provided invaluable insights, continuously offering different perspectives on my research during the oral defense. They also gave me excellent suggestions regarding my thesis and were extremely diligent in guiding me toward the necessary revisions. I sincerely appreciate their commitment and support.

感謝以下實驗室協助進行實驗分析及前處理，並且感謝老師及助理們不厭其煩的指導：蘇志杰老師、徐聖婷助理、張堯禮助理、李紅春老師、羅立老師。

感謝過往曾經在三星妹池進行採樣的工作團隊: 2018 年古湖泊學團隊與 2019 年古湖泊學團隊，特別感謝 Laurin Kolb 提供了許多 2019 年的採樣紀錄與資料。感謝三星妹池採樣小隊，Ludvig Löwemark, Romy Ari Setiaji, 廖倩儀在我採取研究樣本時給予我相當多的協助。並且我還要感謝 2021 年古湖泊學工作團隊，協助進行湖泊演育過程的理論建立，以及提供相當精美的插圖。

感謝林采玟學姊給予我研究上的解惑以及精神上的鼓勵，儘管我的問題總是相當簡單，但學姊總能隔著時差第一時間回信解答我的疑惑。妳總能用最正確的方法去引導我找出最適合的解釋方法，並不厭其煩的灌輸我正確的研究觀念與想法。甚至在我的口試前幾天，還在與我討論我的實驗結果以及資料解釋上的意義，

doi:10.6342/NTU202304291

堪稱最強救火隊、您就是我臨時抱佛腳的佛腳。

感謝廖倩儀助理在各方面的協助，不僅是在 XRF 的操作與資料分析提供給我相當完整並且專業的解說，更是從生活中的不同例子切入，指導我作為一個合格的碩士畢業生應該具備的能力。舉凡報告時的儀態和說話速度，投影片的完整架構、排版與美編、信件禮儀，以及教導我遇到問題時的處理步驟等相當重要的小事。

感謝簡昱辰陪我在 R308 一起崩潰了整整兩年，儘管我們總是不停地抱怨彼此人生中的種種不順遂，但當我們都完成了各自的研究與任務之後，回頭看才發現原來一切都是過程，我們也成功的贏下了所有挑戰。

感謝實驗室夥伴們這些年來的陪伴，感謝 Akanksha Singh, Romy Ari Setiaji, George Kontsevich, Amy Hsieh、廖倩儀、林采玟、鍾伯均、簡翊展、陳淑俐、簡昱辰、陳信安、呂思瑩、陳宗岱、Kanokpon Surijamorn , Marvin Pöllen，不論是各種餵食、聊天、出野外、文化交流…各位都給予我相當多的快樂，以及研究上的想法與情感上的支持與鼓勵。

感謝地質系男籃的大家給予我在北部也有像家一樣的感覺。每周兩次的練球以及三不五時的隊聚，總是能讓我放鬆平時的壓力，感謝大家願意和學長打球，希望未來還有機會再和大家相聚。

感謝陳詩雅與宮田留佳給予我精神上的支持與鼓勵，是妳們的陪伴與鼓舞，讓我有動力想成為更棒的人、更好的自己。也因為有你們，讓我認識了一群很棒的朋友，總是砥礪著我，要我成為我理想中的那個自己。

再來我想感謝我的家人，感謝我的父母注入畢生資源，栽培我直到碩士班畢業。感謝他們給予我經濟上的資助，讓我能免除後顧之憂的專心在學習的道路上。感謝他們給予我完全的自由，從來不過問我的研究以及進度，當我因課業繁重無法回家時也從不多說兩句，百分之百的相信我，不施加給我過多的壓力，除了感謝還是感謝。感謝我的姊姊在我剛到台北時與我分租家庭套房，讓我在台北也有了實質意義上的家，並時不時給我鼓勵與支持。

最後我想謝謝我自己，謝謝我自己能夠堅持走完這條路。縱使距離再遙遠，沿途風景皆為經過，我也終於穿過了夢之河，看見那片櫻花瓣灑落的綠草地了。

doi:10.6342/NTU202304291

中文摘要

東亞季風帶是全球季風系統中，一個相當重要的子系統。它影響了將近全球四分之一的人口。台灣地處東亞季風系統中，其特殊的地理位置提供了絕佳的條件，使其在時間尺度上研究西太平洋的季風以及颱風等天氣變化之紀錄。然而，從台灣各個湖泊中檢索到之全新世古氣候記錄中存在許多差異。這可能是因為過往的研究中缺乏了湖泊沉積學的觀察，限制了我們對控制湖泊沉積的機制的理解，因此在解釋湖泊記錄時引入了不確定性。

為了解存在於湖泊沉積中的古氣候記錄，必須建立一個可靠的年代模型去解釋隱藏在湖泊沉積物中所顯現出的意義。本研究旨在了解位於台灣宜蘭縣太平山區（24°30'N, 121°35'E, 海拔 2095 公尺）的小型濕地湖泊，三星妹池的湖泊演化過程，以及隱藏在湖泊沉積物中之意義。本研究透過鑽取湖泊岩心作為主要的研究材料。使用來自溼地中不同位置的多個沉積岩心，包括已經被草木覆蓋的樹林沼澤、緊鄰水邊之沼澤區和池子中，等各種不同的沉積環境，目的在於建立一個合理的湖泊形成與演化的過程。

本研究於湖泊沉積岩心中應用了多種不同的分析指標，包含:碳 14、鉛 210、銫 137 等定年分析，總有機碳和總氮量分析，生物指標分析，與 X 射線螢光光譜分析(XRF)。然而，來自濕地不同部分的岩心在經過多種的實驗方法中，發現了年代與沉積速率存在了令人困惑之差異。由多個放射性碳 14 定年測定的結果證實了這種倒轉並不是由於採樣之人為因素或是實驗分析偏差，而是真實反映了沉積序列的逆轉。可能解釋這種年代反轉的假設包括人為採樣疏失，浮島的翻轉，山崩等。臺灣其他山區湖泊的案例顯示，由水生植物、苔蘚植物和沉積物混合而成的浮島在颱風期間可以移動數百米。如果浮島翻轉，可能會導致反轉之年代序列。建立的穩健年代模型和湖泊演替模型將對後續的氣候研究有所幫助。

關鍵字： 湖泊學、古湖泊學、湖泊沉積物、湖泊形成、湖泊演替

doi:10.6342/NTU202304291

Abstract

Monsoon rainfall in East Asia is a subsystem of the global monsoon system and affects nearly one-quarter of the world's population. Taiwan, an island in the subtropical East Asian monsoon system, provides the unique opportunity to study monsoon and typhoon variability over the western subtropical Pacific on both historical and geological time-scales. However, the Holocene paleoclimate records retrieved from various lakes in Taiwan have shown discrepancies in their recorded climate variability. This could partly be caused by the lack of modern sedimentological observations, limiting our understanding of the mechanisms controlling lake sedimentation and thus introducing uncertainty in the interpretation of lake records.

The aim of this study is to understand the complex processes that led to the formation of a small wetland, Sanxingmei Pond, which is located in the Taiping Mountains, Yilan County, NE Taiwan. (24°30' N, 121°35' E, 2095 meters above sea level). This study shows how lake succession can explain differences in lithology between nearby coring sites. Moreover, the study emphasizes the need for robust age models to understand paleoclimate records archived in lacustrine sediments. Convoluted sedimentary layers caused by floating islands are hypothesized as the

doi:10.6342/NTU202304291

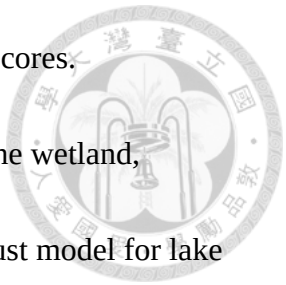

preferred explanation for significant age reversals observed in some cores.

This study uses several sediment cores from different parts of the wetland, including wooded swamps, fens, and open ponds, to construct a robust model for lake formation and succession. A multi-proxy approach was applied in these cores, including ^{14}C, ^{210}Pb, ^{137}Cs, bulk organic analysis (TOC, TN), and X-ray fluorescence (XRF) data. Cores from different parts of the wetland display puzzling differences in maximum ages and sedimentation rates. Multiple radiocarbon dates demonstrate that observed age reversals are not a sampling or analytical artifact, but actually reflect an inversion of the sediment sequence. Possible hypotheses explaining age reversals include typhoons, landslides, and overturned floating fens. Other mountain lakes in Taiwan provide examples of these floating islands where a mixture of aquatic plants, bryophytes, helophytes, and sediment can move hundreds of meters during typhoons. If a floating island is blown by typhoon winds it may become overturned, resulting in an inverse age sequence. An improved understanding of age model and lake succession will be helpful for future paleoclimatic research utilizing lacustrine records.

Keywords: limnology, paleolimnology, lake sediments, paleolakes, lake formation, lake succession

doi:10.6342/NTU202304291

Contents

doi:10.6342/NTU202304291

doi:10.6342/NTU202304291

doi:10.6342/NTU202304291

List of figures

doi:10.6342/NTU202304291

doi:10.6342/NTU202304291

doi:10.6342/NTU202304291

List of tables

doi:10.6342/NTU202304291

Chapter 1 Introduction

1.1 Lakes as paleoclimate records

Lakes are a critical natural resource that are sensitive to changes in climate. Over 100 million lakes hold 87 % of Earth's liquid surface freshwater, supporting an international heritage of biodiversity and providing vital ecological benefits. Lakes are also exquisite indicators of local and regional watershed changes, making lakes useful for detecting Earth's response to climate change (Woolway et al., 2020). Lakes are invaluable archives of past climate conditions and environmental changes, making them excellent for studying paleoclimate. These freshwater ecosystems accumulate and preserve sediment layers over time, which contain valuable information about past climatic conditions, vegetation patterns, and human activities. Understanding the origins and morphology of lakes is crucial for interpreting paleo-limnological records and predicting the responses of lake ecosystems to environmental changes, such as climate change and land use modification. One of the primary reasons lakes are suitable for paleoclimate research is their sensitivity to climate variations. Temperature, precipitation, and other climatic parameters can significantly impact lake dynamics, including water levels, sedimentation rates, and biological

doi:10.6342/NTU202304291

communities. These changes leave distinct imprints in lake sediments, allowing scientists to reconstruct past climate conditions accurately. Unlike marine sediments, which reflect broader global climate trends, lake sediments provide information on more localized climate conditions. This is particularly valuable for understanding regional climate patterns, which can vary significantly from global or continental-scale trends. Sediment cores extracted from lakes provide a temporal record of environmental changes, often containing well-preserved organic materials, such as plant macrofossils and microorganisms, allowing for precise sediment layer dating and enabling us to establish accurate chronologies for paleoclimate reconstructions.

1.2. Previous studies

Previous studies have documented the close connection between lake sediments and past environments. These studies have employed various techniques, including sediment coring, lithology, and identification of sedimentary proxies, such as pollens, diatoms, and elemental and isotopic tracers (e.g., Huang et al. (2004) , Selvaraj et al. (2012)) . The findings from these studies have made substantial contributions to our comprehension of historical climate fluctuations, vegetation pattern alterations, land use transformations, and the ramifications of human activities on lake ecosystems.

doi:10.6342/NTU202304291

Numerous investigations in Taiwan have utilized lakes as paleoclimatic archives, focusing primarily on pollen and diatoms (e.g., Lin (2004), Liew et al. (2006), Lin et al. (2007), and Liew et al. (2014)). Researchers often utilized community analysis methods to study diatoms in the lakes of Taiwan. For example, a morphology-based approach has been used to investigate Mystery Lake in Yilan and Liyu Lake in Hualien (Wu and Wang (2009); Wang et al. (2010)). In the later study, Wang et al. identified 50 diatom species in Liyu Lake, including eight newly discovered types. Diatom scholars characterized each species' ultrastructure in detail and inferred the ecological significance of these species within the lake's ecosystem. Fossil diatom assemblages have also been used to reconstruct historical water quality conditions of Great Ghost Lake and Yachi (Wu et al. (1997); Chen et al. (2009)).

In Taiwan, specific studies have been conducted employing chemical analyses of lake sediment components, elemental makeup, and nitrogen and oxygen isotopic compositions. Various dating methods have been utilized, such as carbon-14, lead-210, and cesium-137. For example, Selvaraj et al. (2012) measured total organic carbon (TOC), C/N ratios, and stable isotopes ($\delta^{13}C$ and $\delta^{15}N$) to reconstruct the monsoon climate in Emerald Peak Lake in subalpine NE Taiwan. Lou et al. (1997) used multiple chemical proxies at Great Ghost Lake, the deepest alpine lake in southern Taiwan. They observed distinct white layers in the sediment core, characterized by

doi:10.6342/NTU202304291

lower organic matter content C/P and Si/Al ratios and higher Fe/Mn and Mg/Al ratios. These findings suggest a potentially drier climatic condition, possibly associated with poor watershed vegetation and a lower lake water level.

1.3 Lakes and Ponds

1.3.1 Definition of lakes and ponds

Scholars from different disciplines have different definitions for lakes (Garcia-Castellanos (2006); Williams et al. (2004)), with varying criteria used to describe these bodies of water. In this study, we have established distinctions between lakes and ponds within the context of water body classification, drawing upon the perspectives of Verpoorter et al. (2014) and Holgerson and Raymond (2016). Ponds are characterized as relatively minor water bodies, typically with less than 5 hectares' surface areas, shallow depths not exceeding 5 meters, and emergent vegetation cover typically less than 30 %.

Lakes, functioning as inherent hydrological reservoirs, undergo sedimentation influenced by the influx of diverse materials from surrounding catchment areas (Li et al., 1997). Following their formation, lakes and catchment are impacted by external forces such as weathering, erosion, transport, and deposition (Schleiss et al., 2016).

doi:10.6342/NTU202304291

Most of the lakes gradually fill up with sediment, transforming them into wetlands. Large aquatic plants, like reeds, can accelerate this process and lead to peat deposition (Bornette et al., 1998).

Lakes and ponds are freshwater ecosystems with similarities but also have distinctive characteristics. The relationship between lakes and ponds can be understood in terms of size, depth, ecological factors, and formation processes (Richardson et al., 2022). In general, lakes are more significant and far-reaching than ponds. Lakes tend to have larger surface areas and water volumes, while ponds are smaller. Lakes typically exhibit pronounced stratification, characterized by thermal layers due to water temperature variations resulting from their more significant depth. In contrast, ponds are generally shallower and often lack discernable stratification. This shallowness renders ponds more susceptible to fluctuations in water temperature and dissolved oxygen levels (Korponai et al., 2010).

1.3.2 Subtropical high mountain lake

High mountainous lakes receive water from precipitation, streams, rivers, snowmelt, and groundwater and their clarity and color vary depending on local geology and vegetation. Mountainous lakes vary in size and depth, supporting unique ecosystems and local biodiversity (Xing et al., 2005). Subtropical (23.5°N - 23.5°S) high-mountain lakes represent a distinct classification of lakes, typically influenced by

doi:10.6342/NTU202304291

warm to hot temperature regimes and exhibit notable wet and dry seasons. The water quality of these lakes is notably affected by the abundant and dense vegetation that typically surrounds them (Havens et al., 2004).

1.3.3 Lake sediment

Lake sediment is derived from diverse sources within and outside the lake system. The principal contributors encompass erosion in the catchment, river inflow, biological activity, atmospheric deposition, and anthropogenic influences (Dearing, 1991). Natural processes, such as rock and soil weathering, alongside human-induced activities like deforestation, agriculture, and construction, contribute minerals, organic matter, and debris from upstream catchments which is transported by rivers and deposited into the lakes. Leng and Marshall (2004) emphasize that biological activity, notably organic matter production by aquatic flora and algae, further contributes to sedimentation within lake systems. Over time, this organic matter, including deceased plant material and algal blooms, settles at the lake bottom. Atmospheric deposition, characterized by particulate matter and pollutants, constitutes an additional lake sediment source.

doi:10.6342/NTU202304291

1.4 Objective

In the context of Holocene climate fluctuations, the task of identifying diverse paleo-environmental indicators presents considerable challenges. While sediment cores characterized by uninterrupted sedimentation and consistent sedimentation rates hold the potential to provide insights into climate shifts within the region, research has frequently disregarded crucial aspects, namely the typology of lake sediments and lake developmental processes.

Sanxingmei Pond, situated in the Taiping mountains, Yilan area, is located at an important geographic position. The convergence of the Northeast monsoon during winter and typhoons in summer renders the locale highly responsive to climate variations. Given the scarcity of lakes in Taiwan, even imperfect climate archives are valuable. Consequently, it is essential to fully understand lake formation and succession processes as a prerequisite for undertaking paleoclimate reconstructions.

doi:10.6342/NTU202304291

Chapter 2 Background

2-1 Geological setting

This study was conducted in Sanxingmei Pond, which is located in Taiping Mountain, Yilan County, Taiwan (latitude 24°30'57.0", longitude 121°35'21.6" (TWD97) (Figure 1A&B). The altitude of the Taiping Mountains ranges from 300 meters to 2,500 meters. Due to the temperature lapse rate of about 6 degrees per kilometer, the altitudinal zonation of the mountain area results in several distinct types of forest, from subtropical rainforest, warm-temperate forest, to subalpine coniferous forest (Lin, 2009). The research site has an elevation of approximately 2100 meters and encompasses a small lake basin. Positioned within an expansive wooded wetland area framed by steep slopes, the current pond features a central open expanse spanning approximately 300 square meters. Notably, the pond's water level undergoes minimal changes during the winter and summer. Based on the definitions of lakes and ponds in Chapter 1-3-1, as the depth and surface area fall within the criteria defining a pond, this study classifies Sanxingmei Pond as a pond rather than a lake. Regarding geographical orientation, the prevailing alignment of the lake follows a northwest-to-southeast direction. A little creek is the primary inflow source on the

doi:10.6342/NTU202304291

southeastern perimeter, and an outflow following the little creek. The catchment area measures 13000 square meters, classifying the site as a miniature forest wetland. Figure 2 illustrates the pond area of Sanxingmei Pond during the winter season.

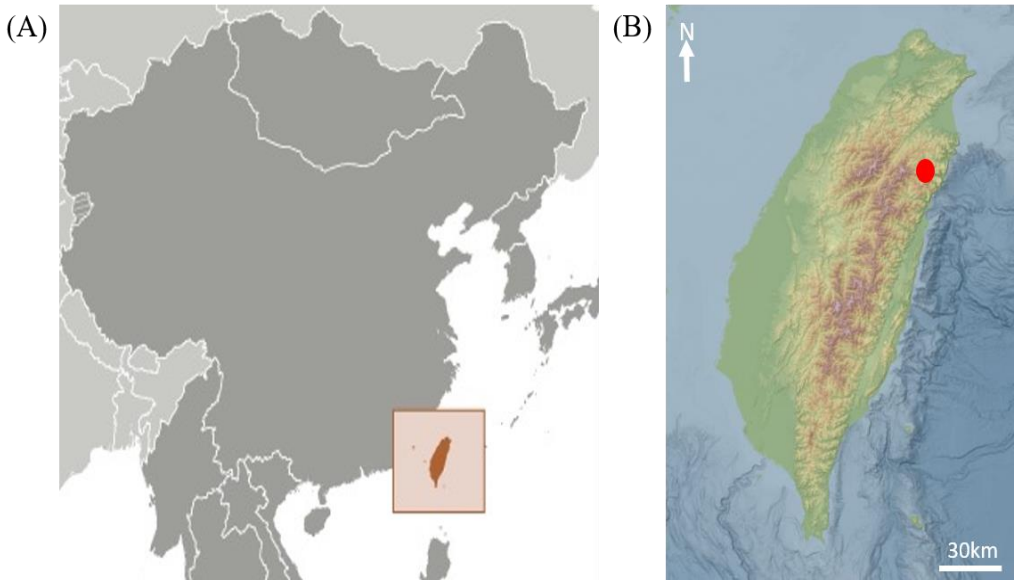

Figure 1. (A) The location of Taiwan (red square) in SE Asia. (B) The location of Sanxingmei Pond (red dot) on the Taiwan map.

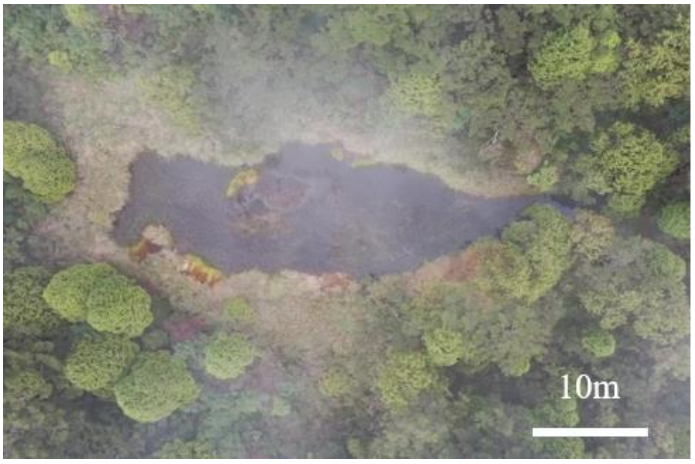

Figure 2. Aerial image of Sanxingmei Pond.

doi:10.6342/NTU202304291

The study area is situated on the western side of the Central Mountain Range and belongs to the Middle Miocene Lushan Formation, Chingshuihu Member. The primary lithology consists of gray-black thick-bedded slate or quartzite, exhibiting well-developed cleavage. Occasionally, thin interbeds or lenses of metamorphosed sandstone can be found. The Sanxing Mountain ridge area predominantly comprises thick sandstones with occasional thin slate layers. Furthermore, approximately 500 meters southeast of the site, a fault known as the Cuifeng Lake fault trends in the northeast-southwest direction.

2-2 Climate features

2-2-1 Overview

Sanxingmei Pond lies within the subtropical monsoon climate zone, with prevailing northeast winds in winter and southwest winds in summer. Because of the steep terrain, the Northeast Asian Monsoon and the winds from the Pacific Ocean are forced upwards, resulting in abundant orographic rainfall, and a relative humidity above 85%. The region's precipitation primarily originates from the Mei-yu (southwest monsoon) rains during spring and summer, as well as typhoons in summer and northeast monsoon in winter (Figure 3). The annual rainfall in the region is 4033 millimeters, with September experiencing the highest precipitation, reaching up to

doi:10.6342/NTU202304291

796.5 millimeters, while March receives the least rainfall, with only 113.5 millimeters.

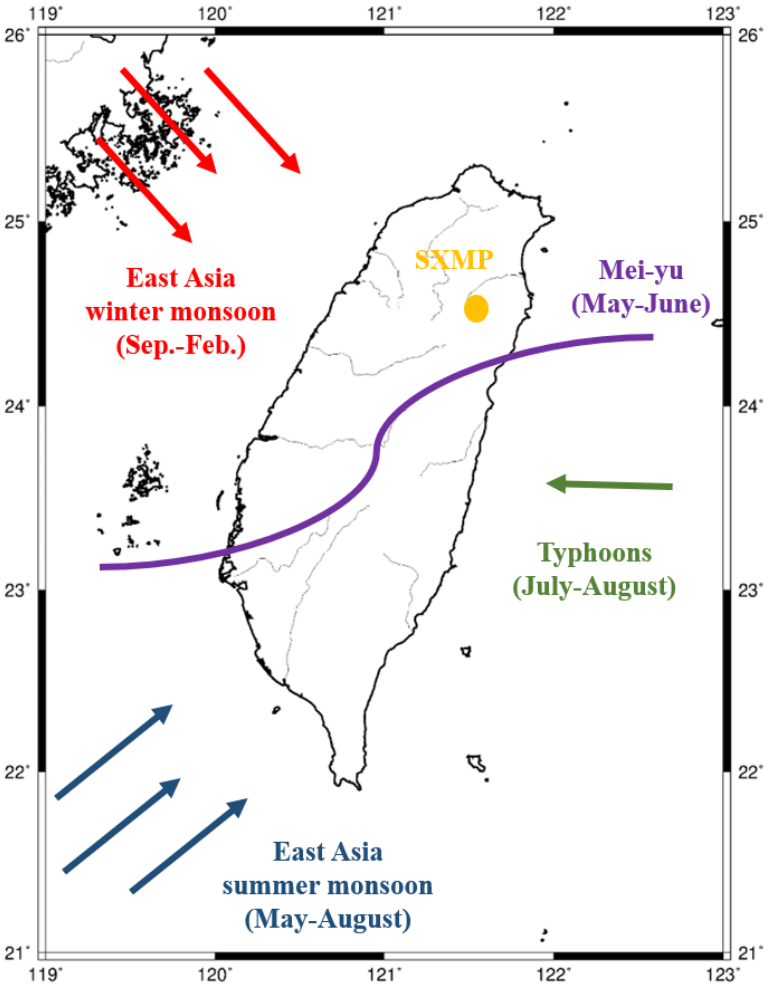

Figure 3. Climate systems that affect the precipitation in Taiwan (Chen & Chen, 2003), including East Asian winter monsoon (red arrows), East Asian summer monsoon (blue arrows), Mei-yu system (purple curved line), and typhoons (green arrows). The yellow dot shows the location of Sanxingmei Pond.

The closest meteorological station to Sanxingmei Pond is the Taiping Mountain Station, located at a latitude of N24°30'19.4" and longitude of E121°31'32.2", with an

doi:10.6342/NTU202304291

elevation of 1942 meters. Meteorological data reveals that the highest average monthly temperature in the Taiping Mountain area occurs in July, reaching 18.8 degrees Celsius. In contrast, the lowest average monthly temperature is recorded in January, with an average of 7.7 degrees Celsius. The annual average temperature is about 11 to 12 degrees Celsius. The coldest months are from November to March, when the average temperature is mostly below 10 degrees Celsius. The lake rarely freezes in winter, but snow is known to fall at elevations above 1800 m from December to February.

2-2-2 Five primary seasons and three types of climatic patterns

The climatic patterns in the region can be categorized into five primary seasons based on their respective sources of rainfall:

1) Winter season (December to February).

2) Spring transition (March to April).

3) Mei-yu season (May to June).

4) Typhoon season (July to August).

5) Autumn (September to November).

The following paragraphs elaborate on the several climate patterns in the Yilan region that contribute to rainfall at the study site: Winter Monsoon, Mei-yu, and

doi:10.6342/NTU202304291

Typhoons.

(1) Winter Monsoon

Monsoon is a climate pattern characterized by an annually reversing wind system (Ramage, 1971). The Asian Monsoon stands out as one of the Earth's most striking climatic occurrences, necessitating local populations to acclimate to the alternating dry and wet seasons influenced by the tropical Pacific and Mongolia air masses (Lau & Li, 1984). Two predominant monsoon patterns significantly influence Taiwan: the northeast monsoon during winter and the southwest monsoon during summer. In our study area, the winter monsoon, with its concentrated rainfall period extending from November through February, is associated with elevated precipitation levels, averaging approximately 2000 millimeters annually.

(2) Mei-yu

The Mei-yu is a feature of the East Asian summer monsoon, which is characterized by prolonged, persistent rainfall, typically from May to June. The rainfall during this period is often substantial, featuring intermittent showers or heavy downpours. Mei-yu rains are controlled by the front between the convergence of cold air masses from Siberia and warm air masses from the Pacific, bringing precipitation

doi:10.6342/NTU202304291

to Taiwan (Chen & Chen, 2003).

(3) Typhoons

Typhoons significantly impact the Yilan region. These powerful tropical cyclones bring heavy rainfall, strong winds, and storm surges, leading to flooding, landslides, and infrastructure damage. The region's topography exacerbates the effects, increasing the risk of flash floods. According to the typhoon warnings published by the Taiwan Central Weather Bureau from 1996 through 2022, Taiwan was subject to 138 warnings, encompassing both offshore and onshore warnings. The annual frequency of typhoons varied between 2 to 9 occurrences. The yearly typhoon-related precipitation in the Yilan region exhibits significant interannual variation, ranging from a minimum of 280.5 mm in 1999 to a maximum of 3620 mm in 2005.

2-3 Classification of lake formation

Lakes encompass approximately 1.8% of the Earth's surface, with a total volume of around 280,000 cubic kilometers of water. Many factors characterize each lake, including water depth, water volume, surface area, catchment area, water temperature, inflow and outflow rates, sedimentation rate, and biodiversity of the surrounding wetland region. Numerous criteria have been established to facilitate the classification

doi:10.6342/NTU202304291

of lakes, incorporating aspects such as productivity the lake's duration, and its mode of formation (Downing et al., 2006). However, this study will follow Hutchinson and Edmondson (1957)'s idea to propose a classification system comprising 11 distinct major types of lake formation. Table 1 shows the 11 distinct lake types of lake formation.

Table 1. The eleven major types of lake formation. Modified from (Hutchinson & Edmondson, 1957).

Lake types	**Description**
1) Tectonic lakes	Tectonic lakes, renowned for their exceptional depth and size, arise from the tectonic movements of the Earth's crust, such as tilting, folding, or faulting. Example: Dead Sea.
2) Volcanic lakes	Volcanic lakes manifest predominantly within volcanic calderas or craters, or when lava flows obstruct the path of a river or stream (Rouwet et al., 2014). These lakes originate as a consequence of precipitation surpassing the rates of both evaporation and drainage. The absence of distinct inflows and outflows further characterizes their hydrological dynamics. Example: Lake Coatepeque, El Salvador.
3) Landslide lakes	The blockage of a river valley creates a landslide lake by either mudflows, rockslides, or debris flow. Such lakes are most common in mountainous regions and are also known as debris dams or barrier lakes. Example: Usoi dam, Tajikistan.
4) Glacial lakes	Glacial lakes, the most abundant type of lakes worldwide, originate directly from the impact of glaciers and continental ice sheets (Carrivick & Tweed, 2013). An example of a glacial lake is a proglacial lake. Proglacial lakes materialize near a glacier's terminus, resulting from the accumulation of meltwater within the space between the glacier and the newly exposed land. Example: Lake Algonquin, United States.
5) Solution lakes	A solution lake is formed when the bedrock is soluble, and the dissolution of the bedrock by percolating water results in the formation of hollows or

doi:10.6342/NTU202304291

	depressions that can give birth to a lake. The precipitation accumulation in the depression can fill it up to create a lake. Also, if the soluble bedrock collapses to form sinkholes in a region where groundwater is close to the surface, the water can fill up the sinkhole creating a solution lake. Example: Muttsee, Switzerland.
6) Fluvial lakes	Lakes formed by the course of a river, known as fluvial lakes, display winding patterns owing to the uneven and diverse landscape of the surrounding terrain. Among the notable fluvial lake types are oxbow lakes and floodplain lakes. Example: Carter Lake, United States.
7) Aeolian lakes	Lakes produced by the wind are known as Aeolian lakes. These lakes commonly emerge in arid settings, often within deflation basins, which persist due to recurring deflation events and sediment buildup in adjacent areas (Stauch, 2015). Example: Moses lake, United States.
8) Shoreline lakes	Shoreline lakes are formed along the coastline or between islands and the mainland. The interaction between rivers and ocean processes creates the depression filled with water separated from the sea.(Boak & Turner, 2005). Example: Shoreline Lake, Palo Alto, California.
9) Organic lakes	Organic lakes, a relatively rare type, result from the influence of flora or fauna. These small lakes occur in basins associated with beaver dams, coral lakes, or dams formed by vegetation. Example: Beaver Lake, United States.
10) Anthropogenic lakes	Anthropogenic lakes are created by human activity. They can be formed by the intentional damming of rivers or the subsequent filling of abandoned excavations by groundwater, precipitation, or a combination of both. Damming a river or stream is the most common origin of anthropogenic lakes. Example: Lake Taihu, China.
11) Meteorite lakes	Meteorite lakes are formed on land by the impact of extraterrestrial objects onto the Earth's surface. Over the years, rain accumulates in the natural depression, creating a lake. Example: Lonar Crater Lake, India.

doi:10.6342/NTU202304291

Chapter 3 Materials and Methods

3-1 Experimental design

3-1-1 Determination of paleo-wetland area

Given the small size of Sanxingmei Pond (approximately 300 square meters) relative to the wetland area, we aimed to understand the evolutionary processes of the ancient lake by defining the extent of the wetland area in this study. We conducted field observations and GPS measurements of the surrounding topography to outline the boundaries of the paleo-wetland. We identified low-lying regions that likely belonged to the former lake based on constant elevation within the designated area. Furthermore, we employed the spade borer to gain an overview of the sediment sequence in the basin. Yellowish-gray clay and oxidized shale fragments at the base of the extracted cores were used as indicators of the ancient pre-lake river valley boundary and the initial deposition of sediments. This sediment coring technique allowed for a rapid assessment of the size and paleodepth of the ancient lake-wetland system.

doi:10.6342/NTU202304291

3-1-2 Sampling points

Figure 4 illustrates the coring points and the paleo wetland extent determined through the methodology mentioned above. The green area represents our inferred ancient lacustrine basin dimensions, while the blue area delineates the current size of Sanxingmei pond. Purple dots indicate the positions where Russian cores were extracted, while white dots represent the locations where sediment samples were obtained using the spade borer.

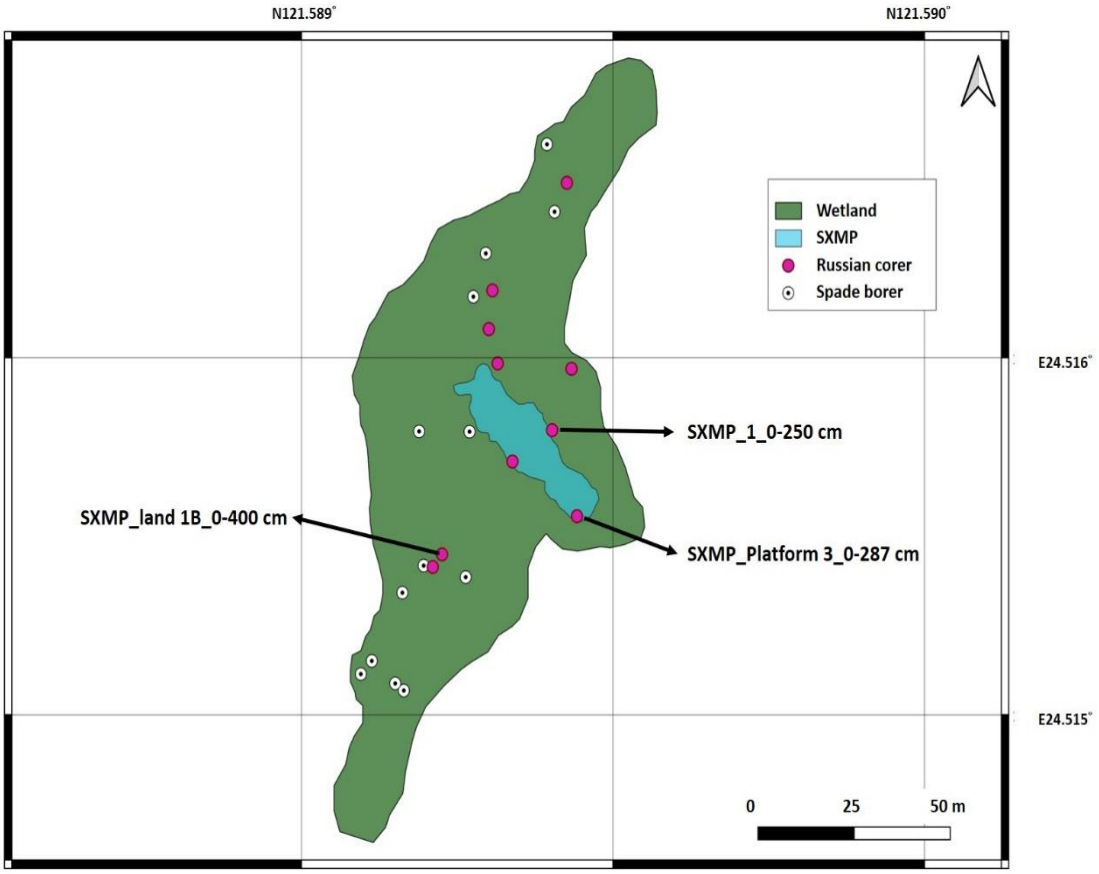

Figure 4. Outline of Sanxingmei Pond. The three highlighted points represent the three primary sediment cores used for this project.

doi:10.6342/NTU202304291

A total of 23 locations in the Sanxingmei Pond-Wetland area were sampled from 2018 to 2021. Among these, 13 points were sampled using the spade borer, while the remaining ten used a Russian corer. Through this array of sampling sites spanning the paleo-wetland, we obtained a broader understanding of the environmental evolution of the ancient lacustrine ecosystem. Table 2 and Table 3 document the sampling timeline and coordinates from the two tools, respectively.

Table 2. Russian corer points. (Cores collected on October 15, 2021, were intentionally limited to 100 cm, prioritizing analysis of upper sediment layers.)

Russian corer

Core ID	Sample latitude	Sample longitude	Sampling date
SXMP_1_0_250 cm	24.51583 N	121.58944 E	2018/09/29
SXMP-Land 1B 0-400 cm	24.51555 N	121.58916 E	2019/09/25
SXMP-Platform 3 0-287 cm	24.51564 N	121.58950 E	2019/09/26
SXMP_2021_0726_1B_0-300cm	24.51553 N	121.58913 E	2021/07/26
SXMP_2021_0727_1C_0-250cm	24.51550 N	121.58915 E	2021/07/27
SXMP_2021_0727_2A_0-366cm	24.51606 N	121.58928 E	2021/07/27
SXMP_2021_0728_2B_50-350cm	24.51597 N	121.58949 E	2021/07/28
SXMP_20211016_G3_Site 1_0-50cm	24.51639 N	121.58948 E	2021/10/15
SXMP_20211016_G3_Site 2_0-81cm	24.51615 N	121.58929 E	2021/10/15
SXMP_20211016_G3_Site 3_0-72cm	24.51598 N	121.58930 E	2021/10/15

doi:10.6342/NTU202304291

Table 3. Spade borer points.

Spade borer

Core ID	Sample latitude	Sample longitude	Sampling date
0407-1	24.51525 N	121.58906 E	2021/04/07
0407-2	24.51527 N	121.58904 E	2021/04/07
0407-3	24.51532 N	121.58898 E	2021/04/07
0407-4	24.51529 N	121.58895 E	2021/04/07
0408-1	24.51547 N	121.58905 E	2021/04/08
0408-2	24.51550 N	121.58922 E	2021/04/08
0408-3	24.51553 N	121.58911 E	2021/04/08
0408-4	24.51583 N	121.58910 E	2021/04/08
0408-5	24.51583 N	121.58923 E	2021/04/08
0408-6	24.51632 N	121.58945 E	2021/04/08
0408-7	24.51647 N	121.58943 E	2021/04/08
0408-8	24.51623 N	121.58927 E	2021/04/08
0408-9	24.51613 N	121.58924 E	2021/04/08

3-1-3 Sediment cores used for analysis

To understand the lake succession, a thorough analysis has been undertaken on selected sediment cores. These include SXMP_1, extracted in 2018, and SXMP_land 1B and SXMP_Platform 3, acquired in 2019 as shown in Figure 1. These sampling sites represent distinct developmental phases of the lake succession, such as lake, pond, fen and forested swamp.

doi:10.6342/NTU202304291

3-2 Experiment flow and data collection

3-2-1 Russian peat corer sample curation

The sediment from the Russian peat corers were securely placed in half PVC liners, ensuring a tight seal with a plastic cover. Plastic caps were utilized at the top and bottom of the liner to prevent movement during transport. Subsequently, all the cores were stored at a temperature of 4 ℃ in the ITRAX lab at National Taiwan University.

3-2-2 Core description flow

Upon retrieving the sediment core, it was photographed and a preliminary description of the cores was made before oxidation could influence colors and consistency. Detailed core descriptions were subsequently conducted in the laboratory, preceding the XRF scanning procedure. The core was carefully cleaned using a scraper, and the color and sediment type were recorded. Small samples were extracted using a scraper and compared to the colors on the Munsell color chart to ensure accuracy. Each layer was visually inspected, and its color matched to a standardized color sample on the chart. This standardized approach ensures consistent and objective color classification. In addition to color classification, other visual observations such as sediment texture, layering, and organic material present were

doi:10.6342/NTU202304291

recorded. This systematic approach provides accurate and reproducible sediment core descriptions, facilitating interpretations of sedimentary processes and environmental changes in lake deposits (Schlolaut et al., 2014).

3-2-3 Classification of lake sediment

This study adopts a simplified categorization approach for the cores. As Schnurrenberger et al. (2003) outlined, the classification of lake sediment types is based on visual characteristics including color, discerned viscosity, and the condition of sedimentary components such as leaves and tree roots. The sediments in this study are categorized as herbaceous peat, gyttja, and clay. Subsequent sections provide a more comprehensive description of these three sediment types.

Herbaceous peat (peaty mud)

Peat (Figure 5), an organic material characterized by its soft, earthy composition, consists of identifiable fragments derived from mosses and roots of woody or herbaceous plants and aquatic macrophytes. To categorize the various types of peat, we adopt the primary modifiers proposed by Troels-Smith (1955) and incorporate some of the modifications suggested by Kershaw (1997). Specifically, this study uses herbaceous peat or peaty mud to describe peat samples exhibiting intertwined rootlets, herbaceous plant rhizomes, and stems and leaves.

doi:10.6342/NTU202304291

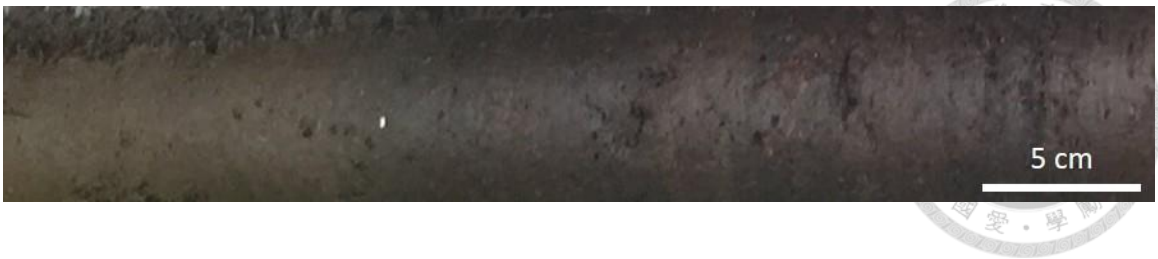

Figure 5. Example of SXMP_Platform 3 of herbaceous peat (peaty mud).

Gyttja

Gyttja (Figure 6), a freshwater deposit in lake bottoms or near shorelines, comprised of organic and mineral materials. The term "gyttja" was initially introduced by Swedish scientist Hampus von Post in 1862 to describe a light-colored deposit formed in eutrophic water bodies (Łachacz et al., 2009). This deposit consists of various components, including plankton particles, pollen, mineral particles, and chitin remains derived from the exoskeletons of insects. Over time, as the peat becomes buried beneath additional layers of peat or soil, the reduced availability of oxygen causes the gyttja to exhibit its characteristic coloration, ranging from olive green to dark brown.

Different research disciplines have employed diverse methods and criteria to define and classify gyttja sediments in sediment studies. It is worth noting that the use of the term "gyttja" has been discouraged by Merkt (1971) due to its frequent misapplication. However, in our study, we followed the perspective presented by Dean (1981), who defined gyttja as sediment containing more than 20 % amorphous organic matter. By

doi:10.6342/NTU202304291

adopting this definition, we aimed to maintain consistency and align our research with existing scientific discourse in gyttja sediment analysis.

Figure 6. Example of gyttja in SXMP_1.

Clay

Clay sediment in lakes can originate from various sources, including erosion and weathering of rocks, transport by wind, streams, and biological activities in the lake (Figure 7). Particle sizes were defined following the Udden–Wentworth scale with clay <0.0039 mm. When fine sediments are delivered into the calm waters of lake basins away from the lake shore, they settle into the lake bed. Clays exist in various colors, black clays containing large concentrations of organic matter or sulfides and whiter clays usually containing high concentrations of calcium carbonate.

Figure 7. Example of clay in SXMP_land 1b.

doi:10.6342/NTU202304291

3-2-4 Sampling tools

This study used two different coring tools for retrieving sediment samples: The Russian corer and the Spade borer. The Russian corer is chosen for its ability to ensure preservation of sediment cores. Its operation may be more complex, but a complete chamber enables the secure storage of collected lake sediment samples. Consequently, the Russian corer is essential when the objective is to preserve sediment cores at designated sampling points accurately.

In contrast, the Spade borer proves valuable in rapidly accessing deeper sites with relative ease. This tool facilitates penetration into the sediment, allowing for swift exploration of subsurface lake sediment variations. The direct drilling approach employed by the Spade borer not only accelerates the coring process but also assists in identifying and selecting optimal sampling points situated at greater depths.

By utilizing the Russian corer and the Spade borer, this study benefits from the combined advantages of proper core preservation and enhanced accessibility to deeper sediment layers. The following section provides a more comprehensive description of these two tools.

Russian corer

The Russian corer is employed to core relatively soft sediment, such as clay, peat, or gyttja (Schnitchen et al., 2006). It can be utilized in proximity to lakes or within

doi:10.6342/NTU202304291

pond environments, and comprises a 1-meter-long steel chamber equipped with a centrally positioned sharp rotating blade, which facilitates the collection of sediment samples into the chamber as shown in Figure 8 (Scott, 2003). Closure of the chamber is achieved by utilizing a T-shaped handlebar at the top. Additionally, the corer includes 1.5-meter-long steel extension rods, enabling the extension of the coring to considerable depths (Pitkänen & Lukasiuk, 2011). When dealing with loosely compacted sediments, manually applied pressure is adequate for inserting the core. However, when the deposit is densely packed and manual insertion is challenging, a handle equipped with a ball clamp can be attached to the rods to facilitate the process.

However, as the corer descends to greater depths, careful attention must be given to the proper connection of new rods. A locking mechanism is employed via screws to secure and release the connection between the rods. It is essential to ensure a tight and secure connection between each rod to prevent the core from becoming trapped within a narrow hole.

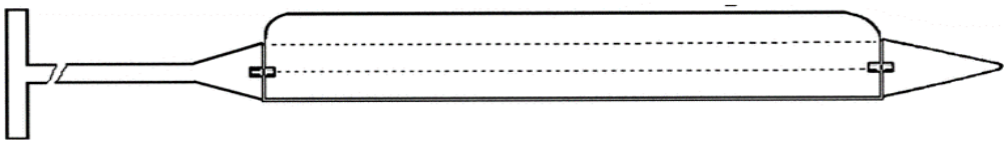

Figure 8. Russian corer (Aaby & Digerfeldt, 1986).

Spade borer

doi:10.6342/NTU202304291

The Russian corer is subject to limitations in terms of maximum depth due to the stiffness and compactness of the sediment. Consequently, an alternative coring tool, the spade borer, was selected for use in this study and primarily designed for rapid drilling and on-site assessment of lake sediment color variations to determine optimal sampling locations for the Russian corer. Unlike the Russian corer, the spade borer does not possess the capability to effectively preserve sediment samples since its chamber remains open during coring operations. The spade borer consists of a rotating handle connected to extendable rods, and its front end features a spiral, open-faced drill bit, enabling swift penetration through compact soil layers and facilitating accessibility to deeper sediment deposits as shown in Figure 9. By employing the extension rods, we inserted the corer into the sediment to the desired depth and twisted it, allowing the open chamber to collect the surrounding sediment. Upon retrieval, the outer part of the corer is cleaned, and observations of the inner sediment are made. The color variations indicate the approximate boundaries between different sediment layers. This characteristic renders the spade borer valuable for penetrating deep and stiff sediments.

Figure 9. Spade borer.

doi:10.6342/NTU202304291

3-3 ^{210}Pb dating

3-3-1 ^{210}Pb dating theory

^{210}Pb dating is a radiometric dating technique that uses the decay of the ^{210}Pb isotope to determine the age of a sediment. It is based on the fact that ^{210}Pb is a product of the radioactive decay of the naturally occurring radionuclide ^{222}Rn, which in turn is derived from the decay of ^{238}U in the Earth's crust. (Figure 10). The use of ^{210}Pb for dating geological and environmental events was first proposed by Goldberg (1963), and soon followed by a study by Crozaz et al. (1964). In the 1960s and 1970s, researchers began using ^{210}Pb to determine sedimentation rates in natural environments by measuring the concentration of ^{210}Pb in sediment cores collected from lake or estuarine sediments.

doi:10.6342/NTU202304291

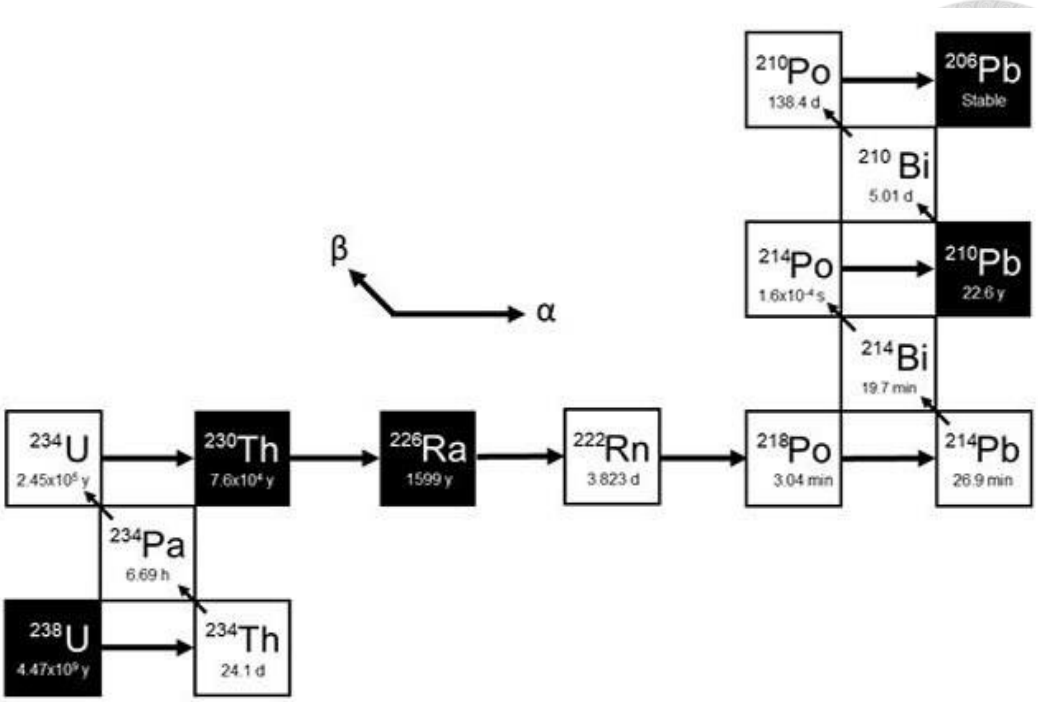

Figure 10. The decay chain of ^{238}U (from Bakri et al. (2021).

The activity of ^{210}Pb is the sum of two sources: $^{210}Pb_{supported}$ and $^{210}Pb_{excess}$. The following explanation will outline the differences between these two and briefly introduce each.

With time, the activity of ^{226}Ra and ^{210}Pb in sediment reaches a state of secular equilibrium, referred to as supported ^{210}Pb. Activities exceeding this equilibrium state are termed excess ^{210}Pb (Goldberg, 1963). Excess ^{210}Pb originates from three pathways: 1. The settling of ^{210}Pb generated from the decay of ^{222}Rn in the atmosphere. 2. Input of ^{210}Pb through riverine transport. 3. Generation of ^{210}Pb from the decay of ^{226}Ra in aquatic systems. Sedimentation rates are computed based on the decay relationship of excess ^{210}Pb over time. Figure 11 shows an idealized curve of supported and unsupported ^{210}Pb.

doi:10.6342/NTU202304291

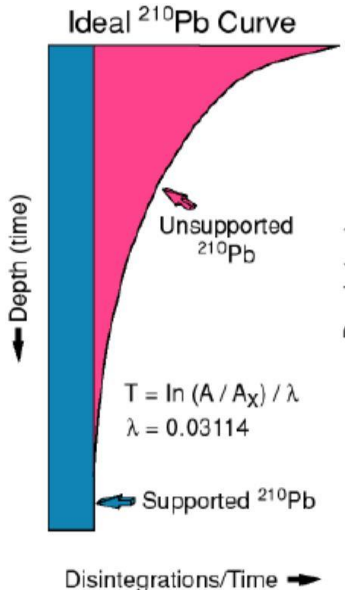

Figure 11. Ideal curve of ^{210}Pb. (Modified from Blake et al. (2007)

3-3-2 Experiment flow

Our analysis was conducted at the Institute of Oceanography, National Taiwan University. The measurement and experimental procedure in this study follow the procedures outlined by Huh and Su (1999) and Hsu (2015), with the following steps:

1. Weigh 0.5 g of sediment sample into a crucible and heat the sample at 105 ℃ for > 6 hours to remove moisture, then at 550 ℃ for > 4 hours to remove organic material. Sample are weighed after each step.
2. Add ^{209}Po (40.04 DPM/g, 0.1 ml) as a tracer and weigh the sample again.
3. Heat the Teflon beakers with the sample at 200 ℃ on the heating board with cover. Add HNO_3 (65 %, 5 ml) to remove carbonate for one and a half hours, HF (40 %, 5 ml) to remove silicates, and $HClO_4$ (70 %, 2 ml) to remove organic matter overnight.

doi:10.6342/NTU202304291

4. Cook the liquid until it becomes a light yellow jelly-like precipitate
5. Add 20 ml of distilled water and ammonia solution NH_3(aq) to neutralize.
6. Put the sample into a centrifuge tube, rotating for 3 minutes at 4500 RPM (revolutions per minute).
7. Add HCl (9 N, 2 ml) and distilled water (20 ml), oscillate until homogeneous, and wait one night to dissolve.
8. Add HCl (9 N, 1 ml) into the solution; after oscillating and centrifuging, put the solution on the heating board (90-100 ℃).
9. Add a teaspoon of Vitamin C to reduce Fe^{3+} (the color changes from light yellow to transparent). Put the silver plate into the solution, recording the time for two hours of silver plating.
10. Use acetone and distilled water to wash the silver plate before analysis

After these pre-treatment steps, the alpha particle spectrometer was used to count the ^{209}Po and ^{210}Po activities. The activity of ^{210}Pb involves retrospective inference of the parent nuclide's magnitude via the attainment of secular equilibrium between ^{210}Pb and its progeny ^{210}Po. Following the completion of preliminary processing, adding a known activity of ^{209}Po serves as a tracer. Subsequently, ^{209}Po and ^{210}Po were counted, using an alpha spectrometer. In order to calibrate the decay from the plating time to

doi:10.6342/NTU202304291

the counting time of ^{210}Po, a half-life of 138.4 days was utilized. The resulting calibrated activity of ^{210}Po was then considered total ^{210}Pb activity ($^{210}Pb_{total}$) at the plating time. To determine the excess (or unsupported) ^{210}Pb activity ($^{210}Pb_{ex}$), the background (or supported) ^{210}Pb was subtracted. The calibration of $^{210}Pb_{ex}$ for radioactive decay from the coring date to the plating date was done using the half-life of ^{210}Pb, which is 22.3 years.

3-2-3 Formula for calculating activity

$$\frac{C_{210}}{C_{209}} \times \frac{S_{209}}{W} \times \exp[\lambda^a \times (t_2 - t_1) \times \exp[\lambda^b \times (t_1 - t_0)] = A$$

C_{210}: Counts of ^{210}Po, C_{209}: Counts of ^{209}Po, S_{209}: Counts of the tracer of ^{209}Po

W: Sample weight after adding the HCl

λ^a: Decay constant of ^{210}Po (1.829 yr^{-1})

λ^b: Decay constant of ^{210}Pb (0.0311 yr^{-1})

t_2: Starting time of the machine, t_1: Plating time

t_0: Sampling time, A: Activity of ^{210}Po (equals to activity of $^{210}Pb_{total}$)

All equations are established based on the procedure outlined by Huh and Su (1999), with certain formulaic adjustments made by the work of Hsu (2015) to streamline the process. Figure 12 presents a more intuitive representation of the experimental timeline and the significance of each phase.

doi:10.6342/NTU202304291

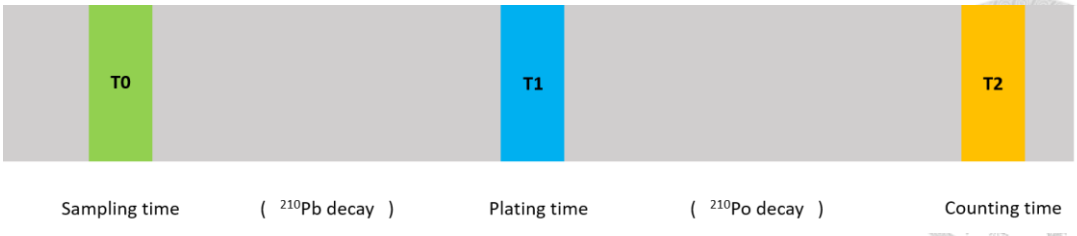

Figure 12. Diagram illustrating the experimental timeline for ^{210}Pb analyses. This is a schematic representation of a time series, where T_0, T_1, and T_2 denote three specific time points as referred to in the equation region above. The remaining gray areas represent the varying levels of radioactivity for the desired measurement of ^{210}Pb and ^{210}Po.

3-4 ^{137}Cs Dating

^{137}Cs has no natural source and is therefore a radioactive isotope widely used in environmental studies to date sediment layers in lakes and other bodies of water. By comparing the amount of ^{137}Cs in a sediment layer to the release of ^{137}Cs into the environment from a known source, such as nuclear weapons testing, we can determine the age of a sediment layer. Due to the signing of the Partial Test-Ban Treaty in 1963 CE, governments worldwide increased their testing activities before the ban, leading to the detonation of their remaining stockpiles of bombs, leading to a peak in the global ^{137}Cs fallout deposition in the Northern Hemisphere during this year. Consequently, many studies have shown that the maximum deposition of ^{137}Cs to lakes and their catchment areas occurred during 1963–64 CE (Pennington et al. (1973);

doi:10.6342/NTU202304291

Appleby (2001); Hirose (2012); Klaminder et al. (2012); Lan et al. (2020), which can help us point out the specific year in the dating results.

The laboratory procedures were conducted at the Institute of Oceanography, National Taiwan University. All experimental steps adhered to the protocol outlined by Ritchie and McHenry (1990).

The procedure for determining ^{137}Cs via gamma spectroscopy encompassed a series of sequential stages. The sediment samples were prepared by freeze-drying and subsequent comminution into a fine powder. Subsequently, the prepared samples were introduced into a specimen receptacle. The gamma spectrometer was then employed to detect and quantify the gamma ray energies emitted from the sample. Emissions of gamma rays possessing an energy profile unique to ^{137}Cs were detected. The gamma spectrometer detected and recorded their energies and intensities. Through an assessment of the energy levels and intensities of the gamma rays emitted by the ^{137}Cs present within the samples, the amount of ^{137}Cs within the sample was determined.

3-5 Radiocarbon dating

3-5-1 Background of Radiocarbon dating

Late Quaternary lake chronologies are commonly based on AMS ^{14}C dating of bulk sediment and plant macrofossils (Hatté & Jull, 2015). The origin of natural

doi:10.6342/NTU202304291

radiocarbon (^{14}C) can be traced back to the upper atmosphere where thermal neutrons, generated by cosmic rays, collide with nitrogen atoms. Following their production, ^{14}C undergoes β-decay, gradually transforming into ^{14}N.

The rate of decay is determined by the ^{14}C half-life. In this study, we apply Cambridge half-life of 5730 ± 40 year (Godwin, 1962), which is thought to be an accurate reflection of the true decay rate. Radiocarbon dating is calculated through the following steps: The β-counting method measures the sample's radioactivity, while accelerator mass spectrometry determines the isotopic ratio of carbon. Both measurement values must be converted based on the isotope fractionation effect to align with measurements from contemporaneous woody samples. Since the $\delta^{13}C$ of woody samples is known, substituting the converted measurement values into the following formula yields the radiocarbon age: -8033 • ln (Fm) (McNichol et al., 2001) . It is important to note that this calculation used the Libby half-life of 5,568 yr BP (Libby & Johnson, 1955), rather than the more precise modern measurement value of 5,730 yr BP. This deviation will be subsequently calibrated using the Oxcal calibration software.

3-5-2 Sample preparation for radiocarbon dating

The samples for radiocarbon dating were processed in three steps.

doi:10.6342/NTU202304291

1. The dating sample was obtained by picking 0.5 g of organic particles from a one-cm slice subsampled from the core, and storing it in a storage bag.
2. The sample was placed on a sieve with a 500 μm mesh and was rinsed using milli Q and a banister brush until the sediment was removed. Only particles larger than 500 μm were considered useful for dating.
3. The remaining sieved materials were moved to a petri dish and were observed under the Olympus EP-50 microscope.

3-5-3 Protocol for radiocarbon dating sample selection and pretreatment

Leaves and elytra are excellent dating materials since they typically cannot be transported long distances before starting to disintegrate. Roots and wood pieces were avoided because they may have been transported long distances and may be considerably older than surrounding sediment (Stenström et al., 2011). Figure 13 shows examples of the materials used for dating. Following the sample selection protocol, leaves, seeds, barks, and elytras were picked from the sediments and were subjected to pretreatment using an acid-base-acid (ABA) sequence as per the methodology described by Brock et al. (2010).

Samples weighing approximately 5 mg were subjected to pretreatment, involving three solutions at a temperature of 80 ℃. First, to eliminate carbonate, samples were

doi:10.6342/NTU202304291

immersed in 0.5 N HCl. Second, to remove humic and fulvic acids, they were submerged in 0.5 N NaOH. Finally, to neutralize the base from the previous step, the samples were treated again with 0.5 N HCl. After each step, the samples were rinsed with milli Q, and dried in oven at 60 ℃ after the final step. The ABA pretreatment and Accelerator Mass Spectrometry (AMS) radiocarbon dating were conducted at the NTUAMS Lab, Department of Geosciences, National Taiwan University.

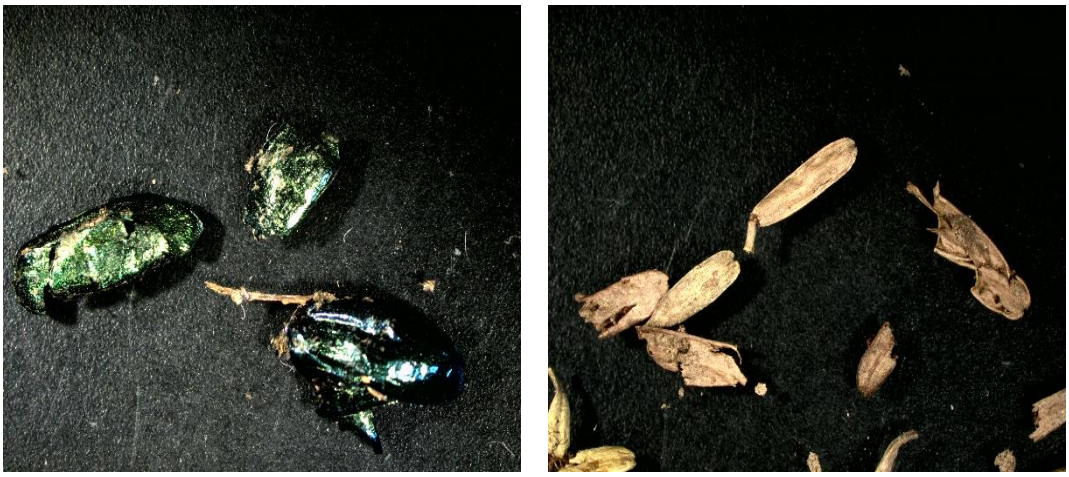

Elytras Leaves and roots

Figure 13. Examples of samples used for radiocarbon dating from core SXMP_Platform3.

3-5-4 Data analysis

Radiocarbon ages were calculated based on ^{14}C counts using the method outlined by Burr et al. (2009). The variations in ^{14}C levels can occur due to a number of factors, such as changes in the Earth's magnetic field, fluctuations in solar activity, and variations in carbon dioxide levels. These variations can lead to inaccuracies in

doi:10.6342/NTU202304291

radiocarbon dating, as the measured ^{14}C levels may not reflect the true age of the sample. To account for these variations, calibration is necessary.

This study uses the Oxcal calibration program to build up a Bayesian-based age model. Figure 14 shows the calibration curve by Ramsey (2009). The calibration process involves comparing the radiocarbon age of a sample to a calibration curve that represents the variation of atmospheric radiocarbon concentrations over time. The calibration curve is constructed using measurements of radiocarbon concentrations in tree rings, corals, and other materials that can be dated accurately using other methods. The curve represents the variation of radiocarbon concentrations over time, which allow us to determine samples' calendar age with greater precision than would be possible using radiocarbon ages alone.

doi:10.6342/NTU202304291

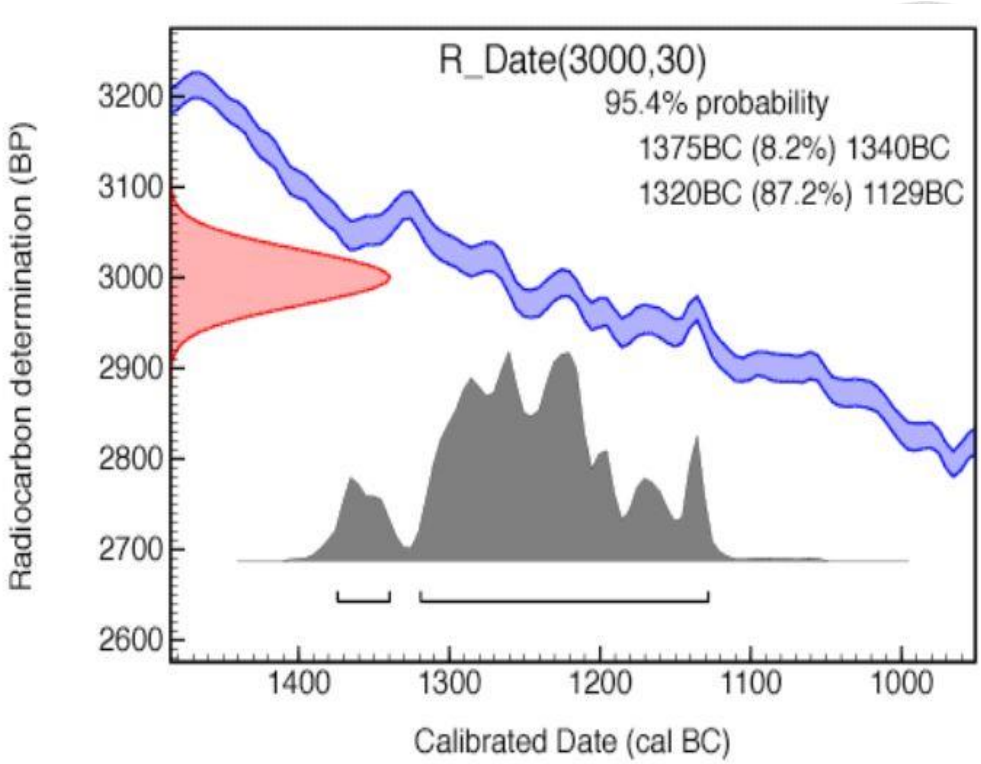

Figure 14. Calibration curve, modified from (Ramsey, 2009).

3-6 X-Ray fluorescence core scanning

X-ray fluorescence analysis (XRF), or XRF elemental analysis, offers a rapid and non-destructive approach to measuring material properties (Croudace et al., 2006). Non-destructive scanners that incorporate XRF analysis have emerged as practical tools for obtaining high-resolution geochemical records from both terrestrial and marine sediment, as well as drilled rock cores (Jansen et al. (1998); Rothwell et al. (2006); Thomson et al. (2006). This method involves exciting fluorescence, referred to as secondary X-rays or characteristic X-rays, from the surface of a sample material using high-energy X-rays. The Itrax XRF Scanner, as depicted in Figure 15,

doi:10.6342/NTU202304291

comprises a central control tower and two lateral compartments for accommodating sediment cores. Cores inserted from the left-hand side undergo scanning within the central control tower before being conveyed to the right half. The internal schematics of the XRF central control tower are illustrated in Figure 16. The analyses were conducted in the ITRAX laboratory at the Department of Geosciences, National Taiwan University. The laboratory is equipped with an Itrax Core Scanner, which consists of a central measuring tower incorporating an X-ray focusing unit and an array of sensors. These sensors include an optical-line camera, a laser topographic scanner, an X-ray line camera for measuring transmitted X-rays, and a high count-rate XRF detection system. The target material utilized in this study was fabricated using the element Mo, known for its stability and ability to provide a series of elemental measurements ranging from aluminum (Al) to uranium (U) within the sample (Croudace et al., 2006).

doi:10.6342/NTU202304291

Figure 15. Itrax core scanner.

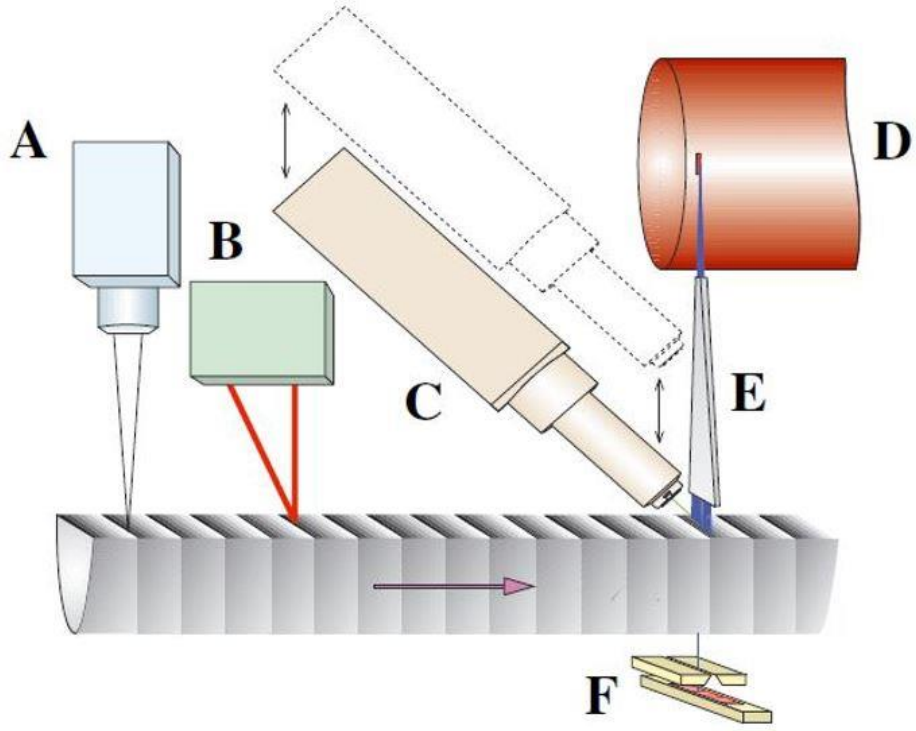

Figure 16. Schematic Diagram of the Itrax Core Scanning System: (A) Optical camera, (B) Laser triangulation system, (C) Mobile measurement system, (D) X-ray tube, (E) Flat waveguide, (F) X-ray camera. Modified from Croudace et al. (2006).

doi:10.6342/NTU202304291

By directing X-rays generated by an X-ray tube onto the sample, electrons from the inner electron orbits of atoms are ejected, creating vacancies in these inner orbits (Beckhoff et al., 2007). To ensure elemental stability, outer shell electrons fill these vacancies as electrons fall to lower orbits, specific energies are emitted. Therefore, the resulting fluorescence differs for each element due to the distinct electron orbits in the inner and outer shells. This characteristic disparity in fluorescence enables qualitative analysis.

Applying XRF scanning when analyzing sediment cores has found broad utility across various research fields, particularly in archaeology, forensic science, and geochemical studies (Liritzis and Zacharias (2011), Kalnicky and Singhvi (2001). Before XRF scanning, the sample pretreatment followed the protocol of Löwemark et al. (2019). The surface of the sediment was meticulously cleaned to eliminate any oxidized coating and ensure a smooth core surface. Subsequently, a protective layer of 2 µm Mylar or polypropylene film was applied to the core to prevent signal bias arising from surface desiccation. The cores were then scanned at a resolution of 200 µm, utilizing a Mo X-ray tube operating at 45 kV and 50 mA, with a measurement time of 5 seconds. Duplicate scans were conducted on a designated section of each core to evaluate data consistency.

doi:10.6342/NTU202304291

Signal bias can potentially arise from various factors, such as changes in grain size within the sediment matrix, mineralogical variations, density effects, and water content (Croudace et al. (2006); Tjallingii et al. (2007). Hence, the raw spectra were subjected to post-processing using Q-Spec 2015 software following the prescribed tuning protocols. The data normalization process follows a series of steps to refine the raw dataset for subsequent analysis. Initially, data points with zero validity are eliminated, followed by removing data points with extremely low counts per second (cps), defined as values below half the average cps within the section. Subsequently, data points exhibiting excessively high Ar/Fe ratios, surpassing twice the average Ar/Fe ratio within the section, are excluded to mitigate the influence of outliers. Further refinement excludes elements with average counts below 60 or zero values accounting for over half of the downcore and Ar records. Additionally, depths with a detection result of zero are removed to ensure the inclusion of only meaningful data points. Normalization progresses by dividing the raw element signal by the sum of incoherent (inc) and coherent (coh) components. After this, the result obtained in the previous step is further divided by the geometric mean values of all remaining elements. Finally, the output is transformed into a natural logarithm (ln) ratio, culminating in a comprehensive data normalization process aimed at enhancing the integrity and comparability of the dataset for subsequent analytical use. In the data

doi:10.6342/NTU202304291

normalization, the procedural steps adopted in this study align with the techniques presented by Lin et al. (2023).

In this study, we use incoherent/coherent (inc/coh) ratios and iron/titanium (Fe/Ti) ratios as indicators of environmental changes. The inc/coh ratio represents the proportion of elastic to inelastic collisions. An increase in incoherence over coherence is correlated with higher organic matter content. This is due to the measurement of incoherent values from light elements such as oxygen and carbon, which are typically prevalent in peat environments. On the other hand, coherence arises from scattering by heavy elements commonly found in the inorganic component. Consequently, this ratio enables an assessment of the ratio of light to heavy elements, contributing to a better understanding of total organic carbon (TOC) abundance (Löwemark et al., 2011).

Meanwhile, the Fe/Ti ratio indicates the sediment's detrital content and degree of weathering. Iron elements are soluble in water, allowing them to be transported into lakes with external inputs. In contrast, due to their low solubility in water, titanium elements tend to be effectively intercepted by littoral macrophytes. Consequently, variations in the Fe/Ti ratio within lake sediments serve as a valuable indicator for inferring changes in the lake's environmental conditions. Variations in the Fe/Ti ratio offer insights into sediment origin within the basin, suggesting that it has been

doi:10.6342/NTU202304291

transported from surrounding areas and deposited within the basin, reflecting a brief transport history (Croudace et al. (2006); Dean et al. (2020). This study employs these two elemental indicators to examine the relationship between TOC abundance, post-transport sediment, and the evolution of the lake basin.

3-7 Total organic carbon (TOC) content analysis

We utilized cores SXMP_1 and SXMP_land 1B obtained during the 2018 and 2019 paleolimnology classes at National Taiwan University. Total organic carbon (TOC) was measured using the Direct TOC Method. This method involves a pretreatment procedure where the sample is subjected to acidification, agitation, and purging to eliminate the Total Inorganic Carbon (TIC) before determining the TOC content.

Core SXMP_Land 1B was analyzed for total carbon (TC), total organic carbon (TOC), and total nitrogen (TN) with a sampling resolution of 10 cm. Dry sediment samples designated for TOC analysis underwent grinding and treatment with 2M HCl (5 ml) for a minimum of 16 hours to eliminate inorganic carbonate, following the protocol described by Schumacher (2002). After thoroughly rinsing with deionized water to remove residual acid, the samples were dried at 55 ℃ and ground again to enhance the reaction surface. Samples for TC analysis were ground and directly

doi:10.6342/NTU202304291

measured without additional pretreatment. The measurements were conducted using an Elementar Vario MICRO cube at the Institute of Oceanography, National Taiwan University. Several standards (Soil calibration material No. 502-309, produced by LECO Corporation) were analyzed to establish a sediment-specific calibration curve and to ensure the performance of the analytical process.

3-8 Biomarker analysis

The analysis of biomarker lipids serves as a proxy to assess changes in the source of organic matter and facilitates the reconstruction of paleoenvironmental and paleoclimatic variations recorded in peat and lake sediments (e.g., Zheng et al. (2007); Yamoah et al. (2016). For this study, sediment core samples were subjected to biomarker lipid analysis, following the pretreatment procedure employed by Yamoah et al. (2016). Measurements conducted as a part of the Palolimnology course at NTU in 2018 and 2019 were utilized to examine the higher plant n-alkane average chain length (ACL), which characterizes the average number of carbon atoms per molecule based on the abundance of odd-carbon-numbered higher plant n-alkanes (Poynter & Eglinton, 1990). Our investigation focused on the influence of vegetation types on the chain length of terrigenous leaf lipids. Notably, leaf lipids derived from grasslands may exhibit longer chain lengths on average than those from forest plants (Cranwell,

doi:10.6342/NTU202304291

1973). Plants are hypothesized to produce longer-chain compounds in warmer climates (Poynter et al., 1989).

To further assess changes in vegetation types, three indexes were calculated. The Average Chain Length (ACL), modified from Simoneit et al. (1991), was employed to identify the relative proportions between grass and forest environments. Additionally, the P_{aq} (Ficken et al., 2000) and P_{wax} (Zheng et al., 2007) indices were used to determine the proportion of aquatic plants relative to terrestrial plants. The formulas for these three ratios are provided below:

$$ACL = \frac{23\times C_{23}+25\times C_{25}+27\times C_{27}+29\times C_{29}+31\times C_{31}+33\times C_{33}}{C_{23}+C_{25}+C_{27}+C_{29}+C_{31}+C_{33}} \quad (1)$$

$$P_{aq} = \frac{C_{23}+C_{25}}{C_{23}+C_{25}+C_{29}+C_{31}} \quad (2)$$

$$P_{wax} = \frac{C_{27}+C_{29}+C_{31}}{C_{23}+C_{25}+C_{27}+C_{29}+C_{31}} \quad (3)$$

The P_{wax} ratio reflects the relative proportion of waxy hydrocarbons derived from emergent macrophytes and terrestrial plants to total hydrocarbons (Zheng et al., 2007). In addition, the P_{aq} index (the aquatic plant n-alkane proxy) is a biological index used to assess aquatic environments. It is calculated based on the sediment's relative

doi:10.6342/NTU202304291

proportions of straight-chain alkanes C_{23}, C_{25} and long-chain alkanes C_{29} and C_{31}. The P_{aq} index provides a means to understand the input of submerged and floating plants (C_{23}, C_{25}) versus terrestrial and emergent plants (C_{29}, C_{31}) in lake sediments. Previous studies have inferred that the range of P_{aq} values in lake sediments represents dominant plant species, where P_{aq} values less than 0.1 indicate dominance of terrestrial plants, P_{aq} values between 0.1 and 0.4 indicate dominance of emergent plants or a mixture of species, and P_{aq} values greater than 0.4 indicate dominance of submerged or floating plant (Ficken et al., 2000).

doi:10.6342/NTU202304291

Chapter 4 Results

4-1 Core descriptions

Detailed core descriptions for the three cores (SXMP_1, SXMP_land 1B, and SMXP_Platform 3) are recorded in Table 4. The colors in the core images may differ from the descriptions in Table 1 due to adjustments during post-processing of the photographs and desiccation and oxidation processes between the time of core description and core photos during XRF scanning.

doi:10.6342/NTU202304291

SXMP_1			
Depth	**Color**	**Sediment type**	**Core description**
0-50 cm	No sediment core preserved.		
50-230 cm	10YR 2/2	Organic rich gyttja	Continuous, no obvious change in the layer.
230-240 cm	2.5YR 7/2	Gray clay	Sticky clay with slate pieces.
240-250 cm	2.5YR 7/4	Yellow clay	More cohesive clay with slate pieces. Noteworthy, from 250 to 200 cm, various sizes of slate pieces are found.
SXMP_land 1B			
0-35 cm	Missing		
35-100 cm	10YR 2/2	Herbaceous peat	No discernible layers or color changes
100-110 cm	10YR 2/1		
110-149 cm	10YR 2/1	Organic rich gyttja	Organic rich horizon, cracks, crumbly, and many roots
149-175 cm	10YR 2/1		No discernible layers or color changes
175-286 cm	10YR 2/2		Same material as matrix, but some light brown specks are admixed. Brown gyttja, organic-rich, wet, and cohesive.
286-296 cm	2.5Y 4/3		Gradual transition zone.

doi:10.6342/NTU202304291

296-300 cm	2.5Y 6/3	Gray clay	Sticky clay with slate pieces.
300-339 cm	2.5YR 7/2		
339-358 cm	2.5YR 7/4	Yellow clay	More cohesive clay with slate pieces.
358-390 cm	5Y 7/1		
390-400 cm	5Y 8/4		
SXMP_Platform 3			
0-30 cm	10YR 2/2	Herbaceous peat	Top 6 cm were half missing. A slightly lighter matrix with black organic particles and numerous elytra was discovered. No discernible layers or color changes
30-136 cm	7.5YR 3/1	Organic rich gyttja	The core exhibits a gradual material transition towards its bottom.
136-178 cm	10YR 2/1		
178-219 cm	10YR 2/2	Gray clay	237-265 cm: There is a significant transition to organic rich gyttja
219-287 cm	5Y 8/4	Yellow clay	

Table 4. The core descriptions for three cores, including information on depth, color, and sediment types.

doi:10.6342/NTU202304291

Figure 17 represents core SXMP_1, with a total length of 250 cm. The core's upper 50 to 0 cm was obtained using plastic tubes directly inserted into the mud, preserving continuous undisturbed sediment. Subsequently, sediment below 50 cm was collected using a Russian Peat Corer, resulting in a total sediment length of 250 cm. Yellow clay is present from 250 to 240 cm depth, while gray clay is observed from 240 to 230 cm depth. The interval from 230 to 50 cm comprises organic gyttja. The lithology and color transition gradually at the boundaries between each sediment type.

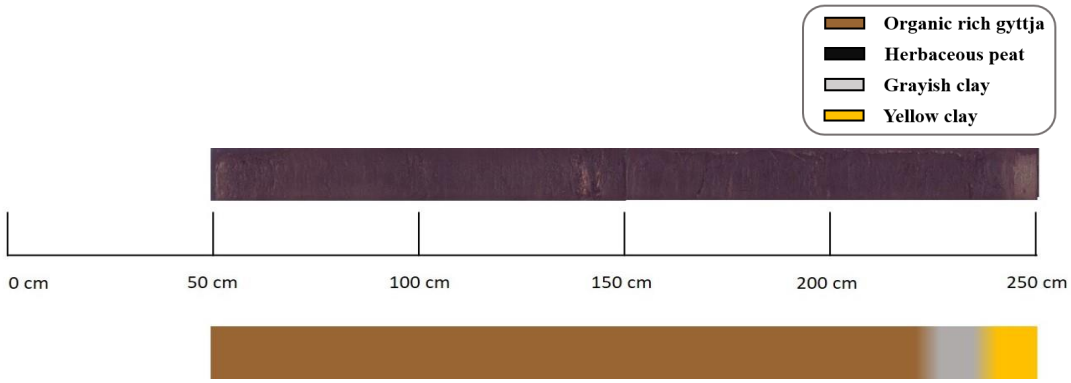

Figure 17. The core image at the top of the figure was taken from XRF optical scanning on SXMP_1, while the types of lake sediment were identified and shown at the bottom.

Figure 18 shows core SMXP_land 1B, the longest of the three cores with a total length of 400 cm, obtained on September 25, 2019. Due to the challenging preservation conditions for the upper 35 to 0 cm sediment, characterized by fluid-like

doi:10.6342/NTU202304291

deposition, this section was not subjected to sample description and analysis. Yellow clay is identified from the deepest part of the core from 400 cm to 339 cm depth, followed by gray clay from 339 cm to 296 cm. The interval from 296 cm to 110 cm, spanning 186 cm, is composed of organic gyttja, while the uppermost 110 cm to 35 cm section corresponds to herbaceous peat. Similar to SXMP_1, slate pieces of varying sizes are found in the deeper clay layers of SXMP_land 1B.

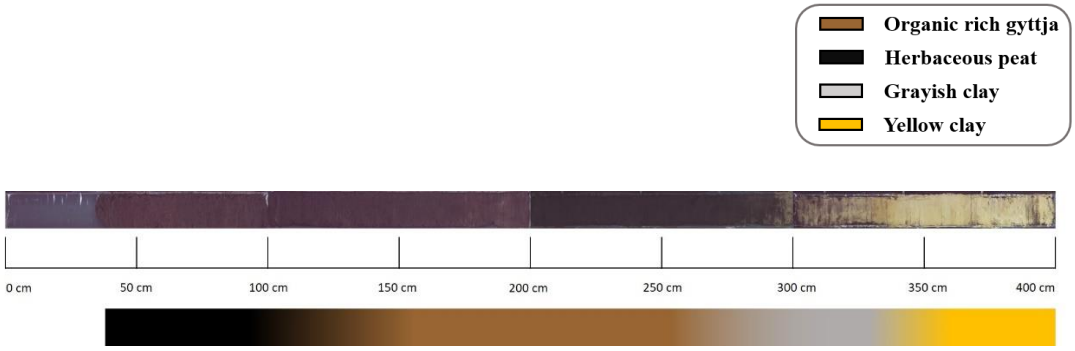

Figure 18. The core image at the top of the figure was taken from XRF optical scanning on SXMP_land 1b, while the types of lake sediment were identified and shown at the bottom.

As shown in Figure 19, core SXMP_Platform3 was collected on September 26, 2019, and had a total length of 287 cm. It is the only core in the study obtained from the open pond. Depth calculation for this core therefore begins upon reaching the lake sediment. The lowermost part of the core, spanning from 287 cm to 219 cm, comprises yellow clay. Then, it transitioned to gray clay from 219 cm to 178 cm.

doi:10.6342/NTU202304291

Between 178 cm and 30 cm, encountered an organic-rich gyttja layer. The uppermost portion of the core, extending from 30 cm to the surface, is characterized by herbaceous peat. The uppermost segment from 6 to 0 cm, where the sediment is relatively soft was disturbed during transport.

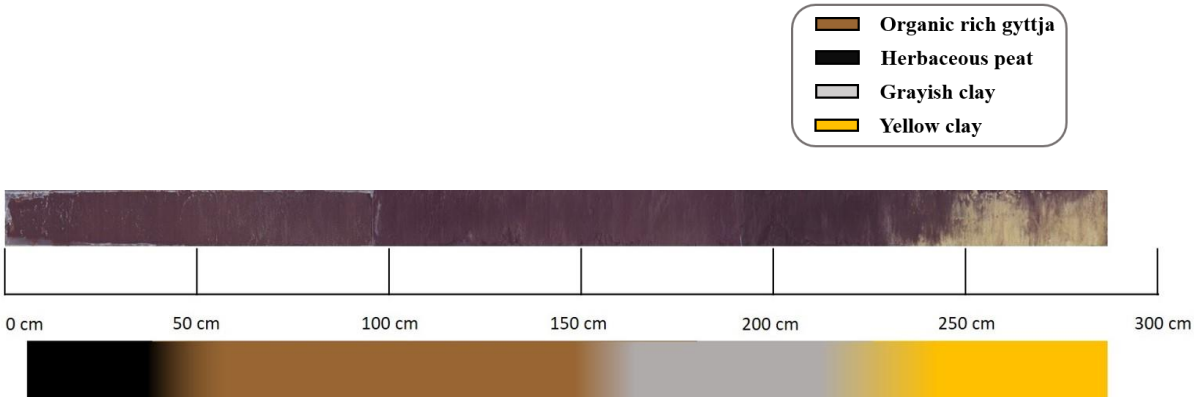

Figure 19. The core image at the top of the figure was taken from XRF optical scanning on SXMP_Platfom 3, while the types of lake sediment were identified and shown at the bottom.

4-2 ^{210}Pb dating results

This study selected three sediment cores for lead-210 dating, SXMP_1, SXMP_land 1B, and SXMP_Platform 3. The excess lead data for the three sediment cores are presented in Table 5, and the variations in excess ^{210}Pb content with depth are depicted in Figure 20.

doi:10.6342/NTU202304291

Table 5. The values of excess ^{210}Pb with depth.

SXMP_1		land 1B		Platform 3	
mid - depth	excess ^{210}Pb	mid - depth	excess ^{210}Pb	mid-depth	excess ^{210}Pb
0.5	30.61	0.5	1.09	6.5	21.04
3.5	33.61	4.5	0.137	8.5	24.04
6.5	15.58	8.5	0.12	10.5	21.19
9.5	4.20	12.5	0.18	12.5	12.81
12.5	2.88	16.5	0.1	14.5	15.54
15.5	3.13	20.5	0.05	16.5	11.4
21.5	3.29	24.5	0.08	20.5	12.9
24.5	1.79	28.5	0.03	22.5	5.16
27.5	2.03	32.5	0.07	26.5	2.76
30.5	0.91			28.5	3.58
36.5	0.69			30.5	1.99
39.5	0.41				
42.5	0.37				

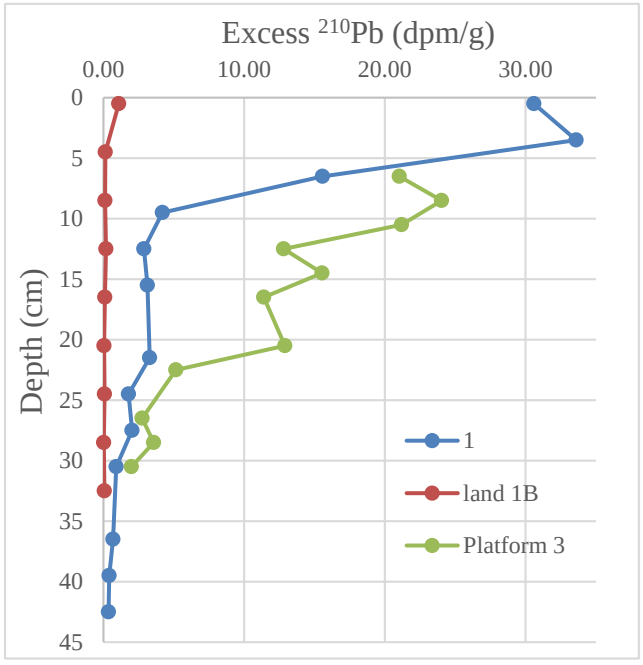

Figure 20. The variations in excess ^{210}Pb content with depth for the three sediment cores.

doi:10.6342/NTU202304291

For SMXP_1, dating experiments were conducted at regular intervals of 3 cm, starting from a depth of 0.5 cm to a depth of 42.5 cm. However, at a depth of 18.5 cm, the sediment sample quantity needed to be increased, resulting in significant measurement errors. Therefore, this data point was excluded from the analysis. In total, 15 results were obtained. The highest excess ^{210}Pb concentration was measured at the uppermost 3.5 cm, reaching 33.61 (dpm/g). Subsequently, the values exhibited an exponential decrease with depth. Notably, at depths of 12.5 cm to 15.5 cm and 24.5 cm to 27.5 cm, higher values were observed, but the trend of excess ^{210}Pb content generally followed an exponential decrease.

In SXMP_land 1B, the measured values were consistently low, indicating the minimal presence of excess ^{210}Pb. Only at the top 0.5 cm, we measured a value of 1.08 (dpm/g), all subsequent measurements were below 1 (dpm/g).

In SXMP_Platform 3, measurements were initiated at a depth of 3.5 cm and conducted approximately every 2 cm, with a few exceptions. Significant measurement errors occurred at 18.5 cm, 24.5 cm, 32.5 cm, and 34.5 cm due to insufficient sample. These data points were considered outliers and excluded from the interpretation of the excess ^{210}Pb trend. At the top 3.5 cm, the 2 cm to 5 cm sediment samples were too sparse, so they were combined and treated as a single measurement at 3.5 cm. The

doi:10.6342/NTU202304291

peak value of excess ^{210}Pb in this core was observed at a depth of 8.5 cm, similar to SXMP_1. The highest measured concentration values of both cores were not from the topmost sediment samples. SXMP_Platform 3 also exhibited several peak inversions at depths ranging from 10.5 cm to 12.5 cm and 16.5 cm to 20.5 cm. Similar to SXMP_1, this core's overall trend of excess ^{210}Pb content showed an exponential decrease.

4-3 ^{137}Cs dating results

The ^{137}Cs analysis in this study focused on SXMP_Platform 3. The purpose of selecting this core was to investigate the contrasting accumulation patterns of ^{137}Cs in open water. This facilitates enhancing the chronological accuracy of the age model employed in this study, yielding the record of the core top.

Figure 21 presents the results from SXMP_Platform 3, which represent an open water setting. Peak occurrence of ^{137}Cs is found between 18.5 and 22.5 centimeters where the values can reach up to 5 disintegrations per minute per gram (dpm/g). No significant changes in peak values were observed at other measured depths. Considering that the peak is likely associated with the 1963 weapons testing (Pennington et al., 1973), this suggests that it corresponds to the year 1963 at a depth of approximately 18.5 to 22.5 centimeters.

doi:10.6342/NTU202304291

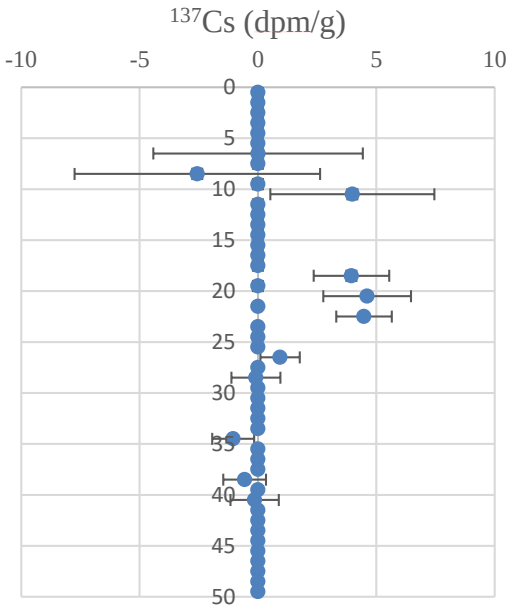

Figure 21. ^{137}Cs dating result of SXMP_Platform 3

4-4 Radiocarbon dating results

Based on the previous chapters, the determination of sampling points and the planning of sampling locations are discussed. Finally, three core samples were selected for radiocarbon dating, namely SXMP_1, SXMP_land 1B, and SXMP_Platform 3, representing three different locations near pond shore, in the wooded swamp and the pond. These three sediment cores represent distinct sampling locations and provide insights into the depositional environments through the data. The sedimentary conditions for SMXP_1 are characterized as gradual deposition. SMXP_land 1b exhibits a pronounced age reversal, and SXMP_Platform 3 is situated within a markedly rapid sedimentary environment.

doi:10.6342/NTU202304291

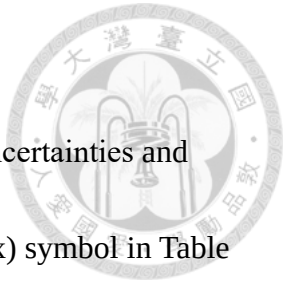

Table 6 presents the chronological data of calibration age with 2σ uncertainties and depths for the three sediment cores. Depth values marked with the (x) symbol in Table 6 signify outliers. Depth designated as outlier exhibit probabilities, as calculated by OxCal, falling below two standard deviations. Consequently, data corresponding to these outlier depths will be excluded when elucidating the age model in subsequent discussions.

Table 6. The radiocarbon dating results after calibration with 2σ uncertainties.

SXMP_1		**SXMP_land 1B**		**SXMP_Platform3**	
Core depth (cm)	**Age (yr BP)**	**Core depth (cm)**	**Age (yr BP)**	**Core depth (cm)**	**Age (yr BP)**
75.5	938 ± 26	86.5	1890 ± 186	154.5	51 ± 102
100.5	2288 ± 194	100.5	1999 ± 188	164.5	196 ± 122
115	2979 ± 168	133.5	2495 ± 200	184.5	219 ± 120
126.5	3087 ± 130	149.5	2642 ± 218	204.5	289 ± 162
143	3264 ± 512	186.5	4137 ± 606	254.5	950 ± 198
177.5	5575 ± 288	220.5	4810 ± 832		
204	7902 ± 314	267.5	5577 ± 680		
221.5	9265 ± 422	270	5615 ± 668		
228	9675 ± 294	276.5	5707 ± 628		
239	11134 ± 488	317.5	6275 ± 198		
		330.5	6482 ± 318		
		339.5	6664 ± 702		
		357.5	7442 ± 972		
		368.5	8057 ± 580		

doi:10.6342/NTU202304291

First, Figure 22 shows the depth vs. dating results plot in core SXMP_1. The depth versus dating results reveals that the simulated ages indicate a sustained deposition rate of roughly 0.016 cm/yr. The sedimentation velocity remains gradual and uniform across all the core samples. Notably, a distinctive interval featuring an elevation in sedimentation rate of about 0.09 cm/yr is discernible during the period spanning 3264-2979 yr BP (143-115 cm depth).

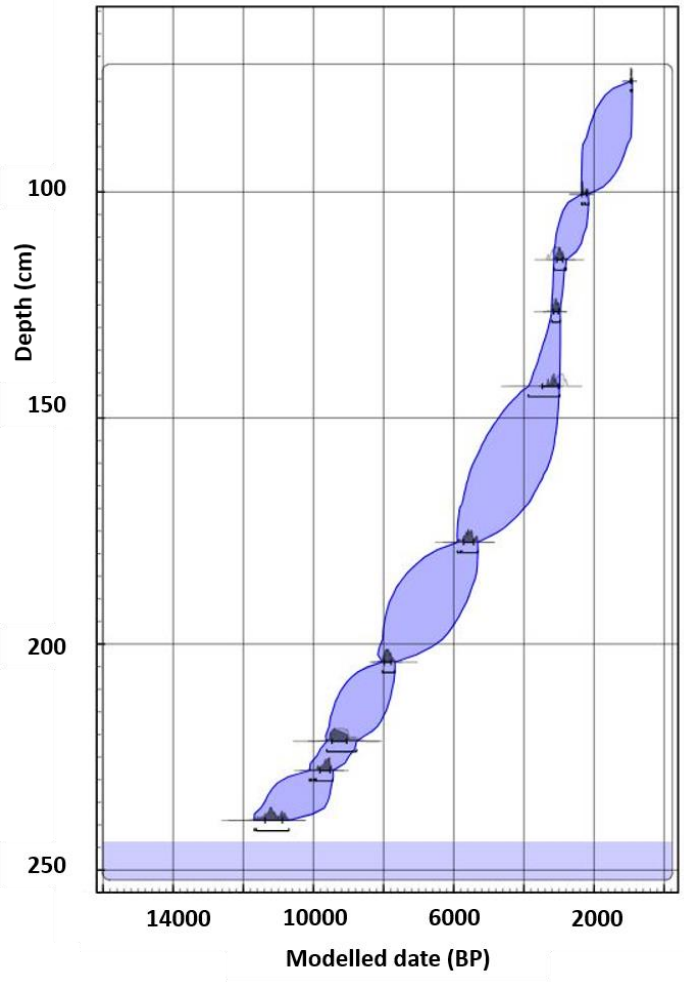

Figure 22. Radiocarbon dating results of SXMP_1. The blue regions signify possible age intervals.

doi:10.6342/NTU202304291

According to the result of Figure 23, we calculated an average annual sedimentation rate of 0.04 cm of SXMP_land 1b. The oldest age was observed at 368.5 cm, corresponding to approximately 8057 yr BP. Guided by observed trends, this core can be reasonably segmented into three distinct depositional stages: firstly, the lower stratum spanning 368.5 cm to 339.5 cm, characterized by a deposition rate of merely 0.02 cm per annum, representing the slowest accumulation phase. The interval from 339.5 cm to 149.5 cm reflects an annual deposition rate of 0.04 cm. Lastly, the upper section, spanning 149.5 cm to 86.5 cm, exhibits a deposition rate of 0.08 cm per year, signifying the most rapid deposition phase within the core. Nonetheless, the detailed radiocarbon dating results for land 1b, considering the presence of outliers, potential stratigraphic inversion, and age reversals, will be reserved for a more in-depth discussion in the forthcoming section dedicated to the discussion.

doi:10.6342/NTU202304291

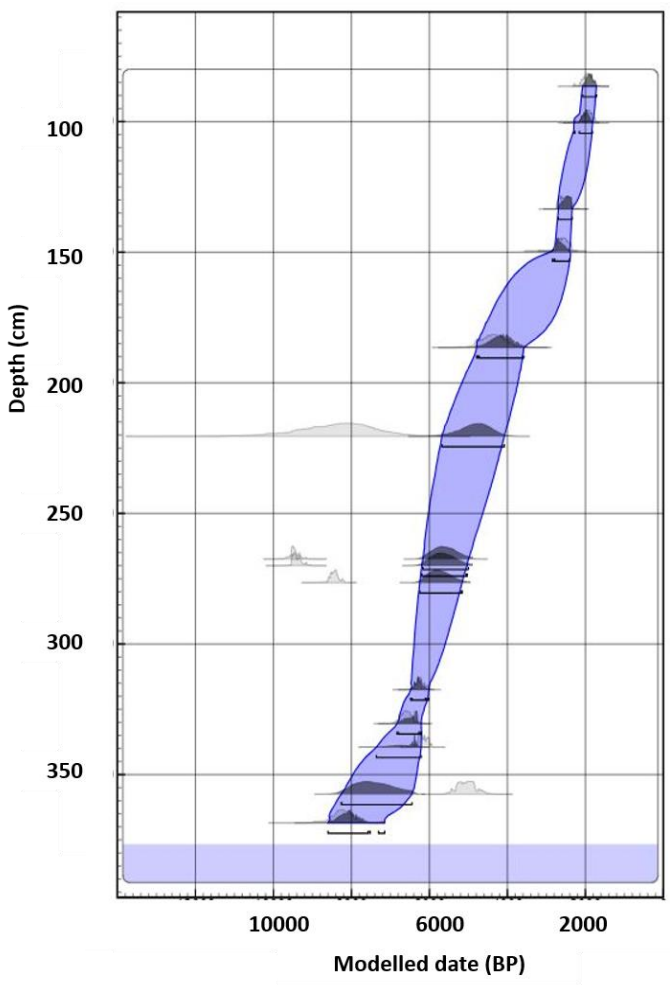

Figure 23. Radiocarbon dating results of SXMP_land 1b. The blue regions signify possible age intervals.

Compared to the preceding two cores, the radiocarbon dating outcomes of SXMP_Platform 3 exhibit relatively young findings. Despite the limited availability of upper sediment samples for analysis, we have ascertained that the most ancient dating results emerge at a depth of 254.5 cm, corresponding to 950 yr BP. Due to substantial computational discrepancies and the absence of samples from the upper sediment layers, no further dating outcomes are available for the uppermost section of

doi:10.6342/NTU202304291

the core. Based on the findings presented in Table 3, we have computed a sedimentation rate of 0.18 cm per year for SXMP_Platform 3. As indicated in Figure 24, the core demonstrates two distinct variations in sedimentation rates: the lower portion from 254.5 cm to 184.5 cm corresponds to a comparatively sluggish deposition (0.1 cm/yr). In contrast, the upper section from 184.5 cm to 88 cm corresponds to a more rapid deposition interval (0.41 cm/yr).

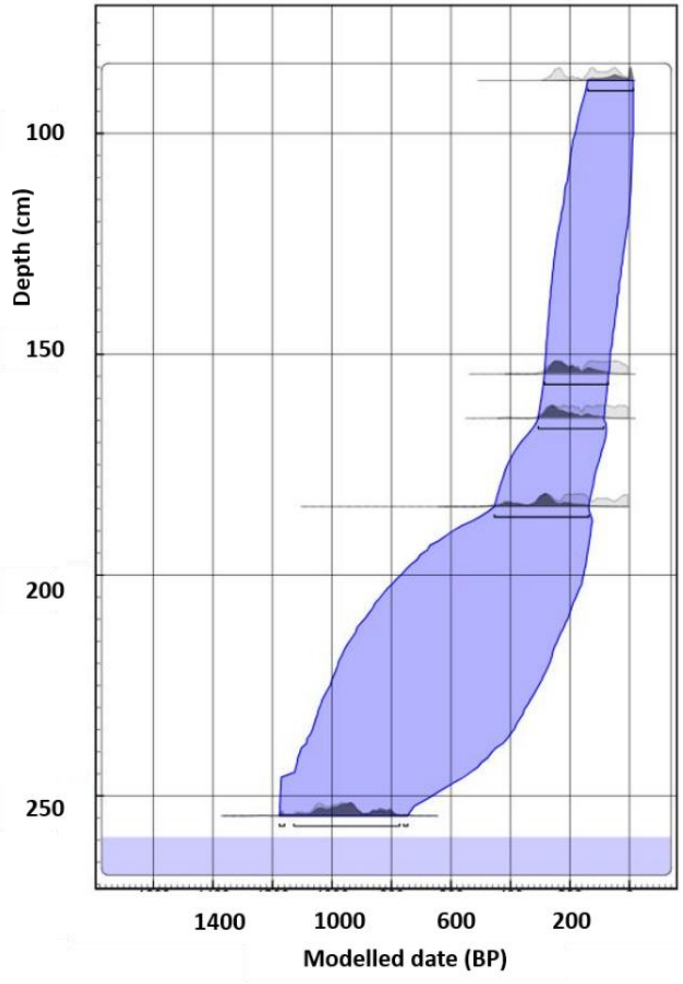

Figure 24. Radiocarbon dating results of SXMP_Platform 3. The blue regions signify the possible age intervals.

doi:10.6342/NTU202304291

4-5 XRF scanning results

In this study, we employed incoherent/coherent (inc/coh), and iron/titanium (Fe/Ti) as indicators for environmental change using X-ray fluorescence (XRF). Increased inc/coh ratio correlates with higher organic matter content, contributing to a better understanding of total organic carbon (TOC) abundance (Löwemark et al., 2011). Meanwhile, the Fe/Ti ratio indicates the sediment's detrital content and degree of weathering, helping us figure out sediment input variability and the evolution of the lake basin.

SXMP_1, with a measurement resolution of 0.5 cm, shows inc/coh, and Fe/Ti values in Figure 25. The inc/coh values on the left side show an overall range between 6.5 and 8, with only a few measurements below 240 cm exhibiting relatively abnormal low values. Conversely, the Fe/Ti results on the right side show a ratio of approximately 0.7 to 0.9, with limited variability even in deeper sections. Both parameters display a downward peak around 205 cm, although between 92 cm and 82 cm, the inc/coh values decrease while the Fe/Ti ratios increase, suggesting a lack of significant correlation between the two.

doi:10.6342/NTU202304291

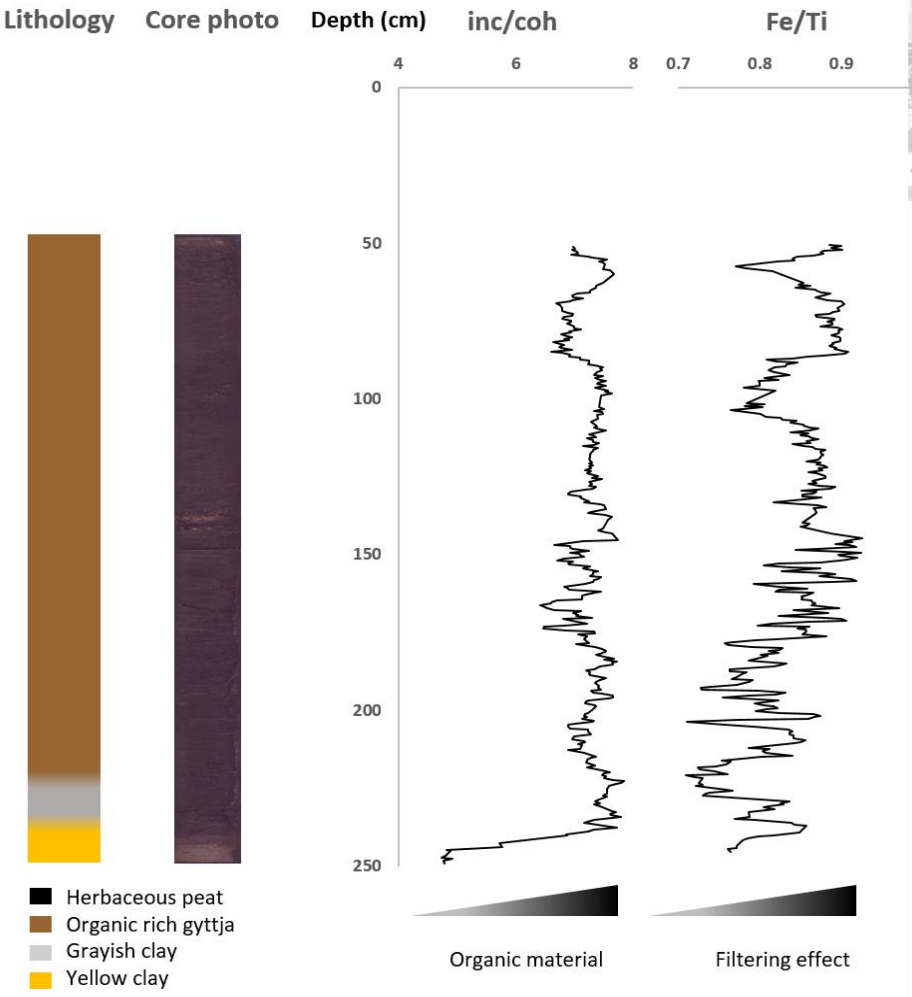

Figure 25. Core lithology, core photo, and XRF results plotted against age for SXMP_1. (No XRF measurement data is available for the top 50 cm of SXMP_1.)

SXMP_land 1b (Figure 26) shows a higher resolution of 0.1 cm per measurement than SXMP_1. The fluctuations in inc/coh values on the left side are greater than those of SXMP_1, ranging between 3 and 8, with a pronounced increase around 275 cm serving as a distinct boundary.

Values before 275 cm are consistently below 4, while those after 275 cm falls

doi:10.6342/NTU202304291

predominantly between 6.5 and 8.2, highlighting a notable shift. The Fe/Ti curve on the right side also reveals an increase of around 275 cm, transitioning from an average of approximately 0.7 to an average of about 0.85, corresponding with the trend observed in inc/coh values.

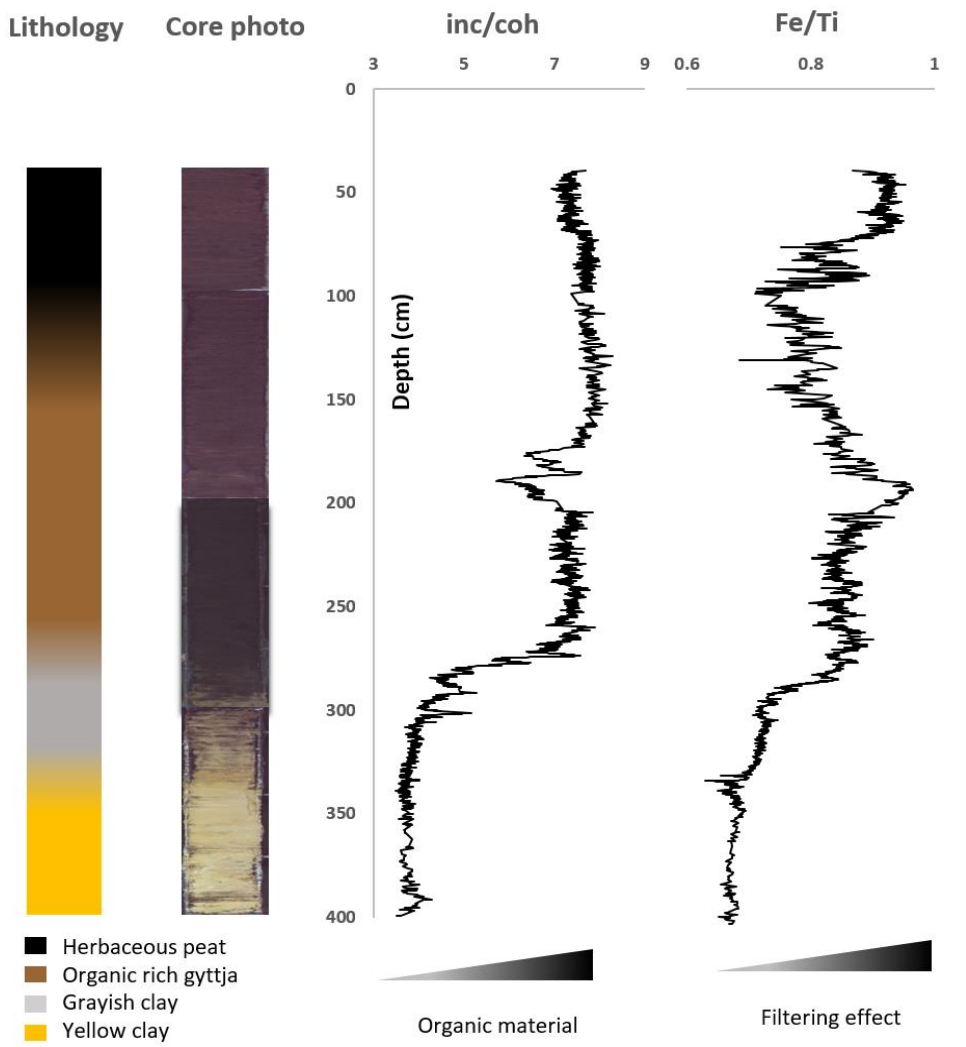

Figure 26. Core lithology, core photo, and XRF results plotted against age for SXMP_land 1b. (No XRF measurement data is available for the top 35 cm of SXMP_land 1b.)

doi:10.6342/NTU202304291

Lastly, in core SXMP_Platform3 (Figure 27), with a resolution of 0.1 cm, Figure 3 shows inc/coh and Fe/Ti results. The radiocarbon dating of SXMP_Platform 3 is derived from deeper sediment layers, and the calibrated dating results indicate its relatively young age, with calculated sedimentation rates leading to negative age values in upper sections. Overall, both inc/coh and Fe/Ti values exhibit an upward trend as chronological proximity increases, with inc/coh values rising from 3 to 7.3 and Fe/Ti values increasing from 0.65 to 0.85. Also, the value of inc/coh and Fe/Ti both show a peak at approximately 211 cm.

doi:10.6342/NTU202304291

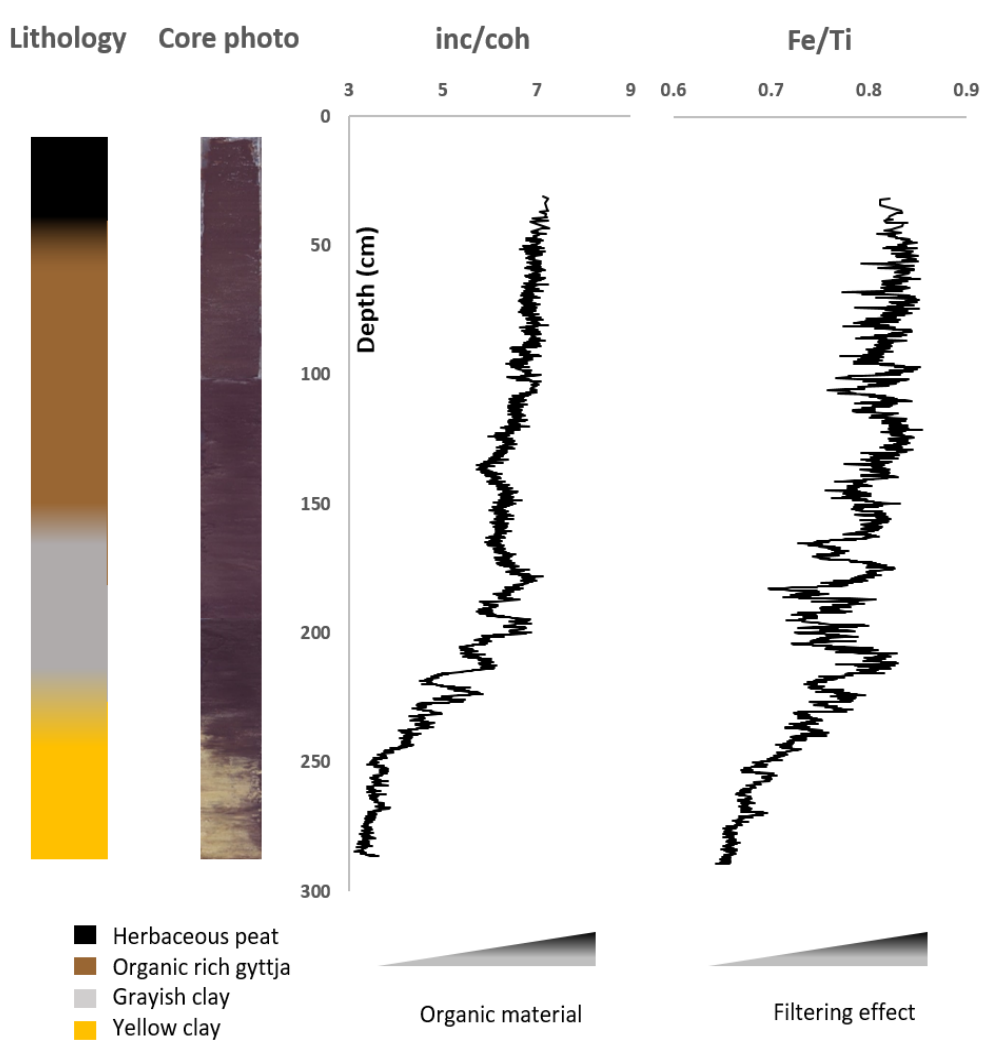

Figure 27. Core lithology, core photo, and XRF results plotted against age for SXMP_Platform 3. (Due to lack of the material, there were no XRF measurement data for the top 31 cm of SXMP_Platform 3.)

4-6 TOC results

Total organic carbon (TOC) and C/N ratios were analyzed in two sediment cores, namely SXMP_1 and SXMP_land 1B, which were obtained during the 2018 and 2019

doi:10.6342/NTU202304291

paleolimnology courses at the Department of Geology, National Taiwan University.

As depicted in Figure 28, the TOC measurements in the SXMP_1 core exhibit values greater than 20 % throughout the core, with an average value as high as 32. Figure 9 further portrays the C/N ratio on the right-hand side, depicting a comparable trend characterized by a progressive decline in values towards the upper portion, albeit accompanied by intermittent fluctuations. The average value for the entire core is 22.16 %. The prominent peaks of C/N ratio occur at 220.5 cm, 176.5 cm, and 128.5 cm, reaching a ratio of 43.4 %, 40.2 % and 36.8 %, also correspond to the TOC (%) peaks. Overall, there is a trend of more significant values in the older section, gradually decreasing upwards.

doi:10.6342/NTU202304291

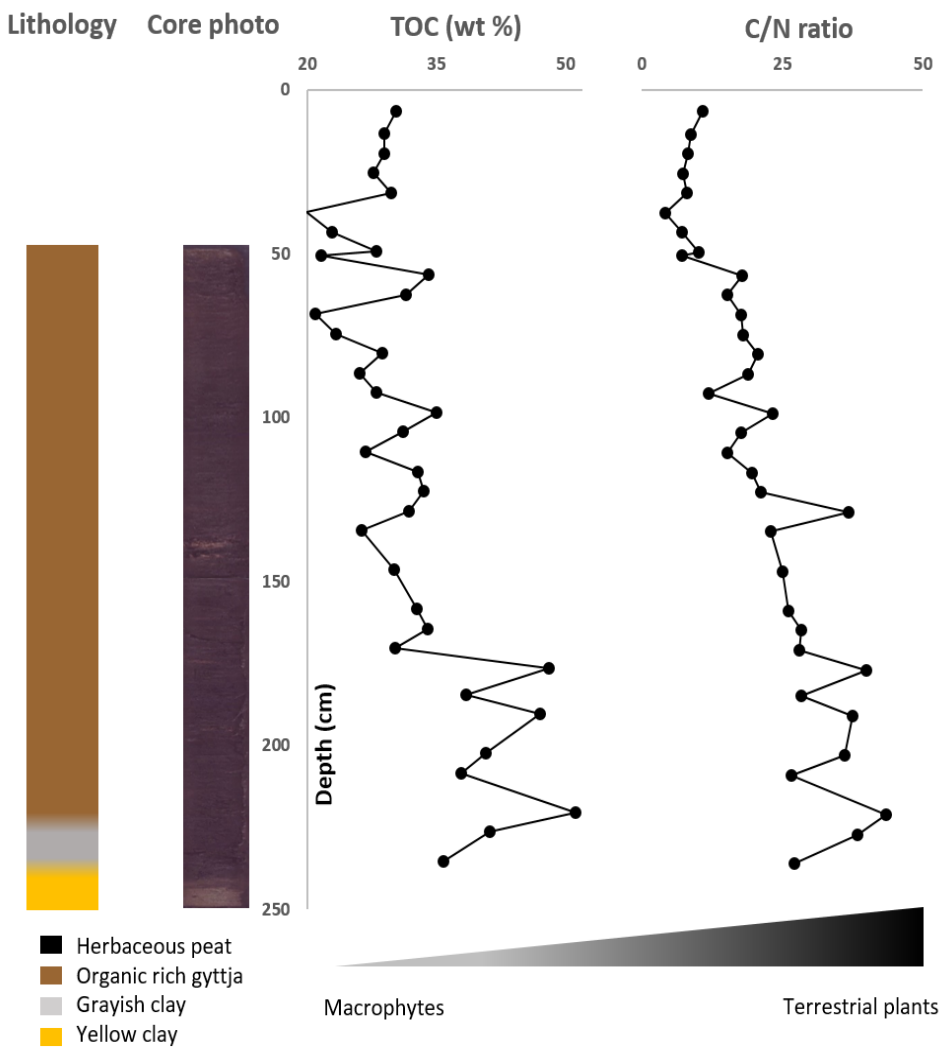

Figure 28. Core lithology, core photo, TOC values (%), and C/N ratio of SXMP_1.

Regarding the TOC results of SXMP_land 1B, as shown in Figure 29, it is noteworthy that values below one are observed in the deepest section, from 394 cm to 284 cm. However, at 274 cm, there is a sudden sharp increase to 21 %. From 274 cm to 224 cm, measurements exceed 20 %, followed by a drop to 11 % at 214 cm. Subsequently, at 204 cm, the measurement rises to 26 %. In the upper part, the TOC values do not exceed 20 % and mainly fluctuate within the range of 7-20 %. Overall,

doi:10.6342/NTU202304291

the trend indicates decreasing values towards upper part. The general trend of the C/N ratio, as depicted in the right hand side of Figure 10, follows a pattern similar to TOC but with some variations. At 264 cm, a measurement of 49.4 is obtained, followed by a decrease to 28.5 at 244 cm. Subsequently, the C/N ratio mostly ranges from 20 to 30, with only one instance below 20 at 59 cm. Despite the prevailing higher value in the upper core section, the average measurement of the C/N ratio stands at a modest 20.6. Furthermore, the average for points measured below 280 centimeters rests at a mere 2.22.

doi:10.6342/NTU202304291

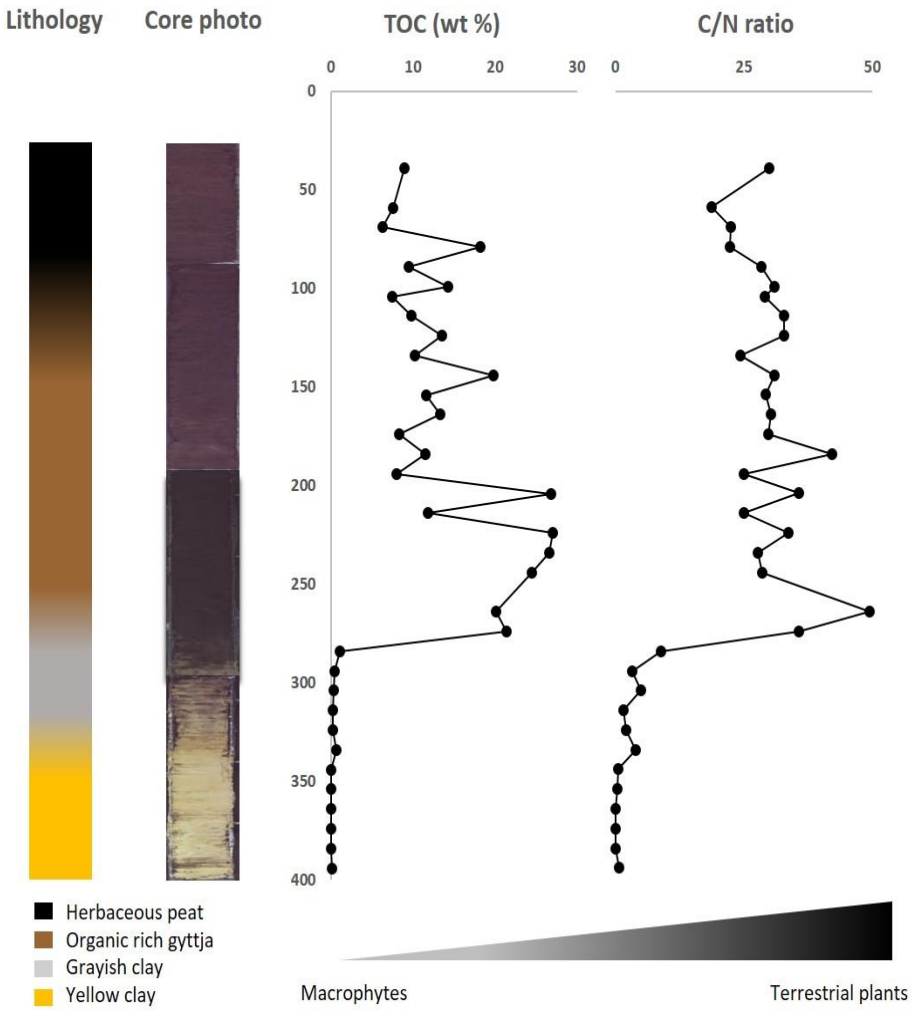

Figure 29. Core lithology, core photo, TOC values (%), and C/N ratio of SXMP_land 1b

4-7 Biomarker results

This study analyzed biomarkers on two sediment cores, SXMP_1 and SXMP_land 1B, and focuses on three specific proxies: average carbon chain length (ACL), P_{wax} and P_{aq}. We assessed the relative distribution of grassland and forest environments by utilizing the Average Chain Length (ACL), a method adapted from

doi:10.6342/NTU202304291

Simoneit et al. (1991). Additionally, the P_{aq} index (Ficken et al., 2000) and P_{wax} index (Zheng et al., 2007) were employed to gauge the ratios of aquatic to terrestrial plant species. ACL and P_{wax} show a positive correlation, while both exhibit a negative correlation with P_{aq}. The x-axis for P_{aq} in this study is reversed to enhance clarity, enabling a more intuitive visualization of the relative relationships among the three proxies.

The results for SXMP_1 are presented in Figure 30, where the ratios ACL, P_{wax}, and P_{aq} are shown from left to right. According to the result, each of the three proxies manifests considerable amplitude variations within the lower stratum while revealing a comparatively consistent signal within the upper stratum. The average ACL for SXMP_1 is 26.68. The core's bottom section displays significant variability, ranging from below 26 to above 28, stabilizing between 26 and 27 above 134.5 cm. Two distinct peaks are evident at 190.5 cm and 146.5 cm, with values of 28.14 and 27.98, respectively. Additionally, noticeable low values are observed at 208.5 cm and within the interval from 184.5 cm to 170.5 cm, with measurements ranging from 25.94 to 25.86. P_{wax} generally correlates with ACL, exhibiting significant variability in the deeper sections, becoming relatively stable above 134.5 cm, with an overall average value of 0.65. Like ACL, P_{wax} presents clear peaks at 190.5 cm and 146.5 cm, with values of 0.88 and 0.96, respectively. The average P_{aq} value is approximately 0.54.

doi:10.6342/NTU202304291

Notably, low values are found at 190.5cm and 146.5 cm, with measurements of 0.13 and 0.05, respectively. The values in the upper section remain relatively stable, ranging from 0.4 to 0.7.

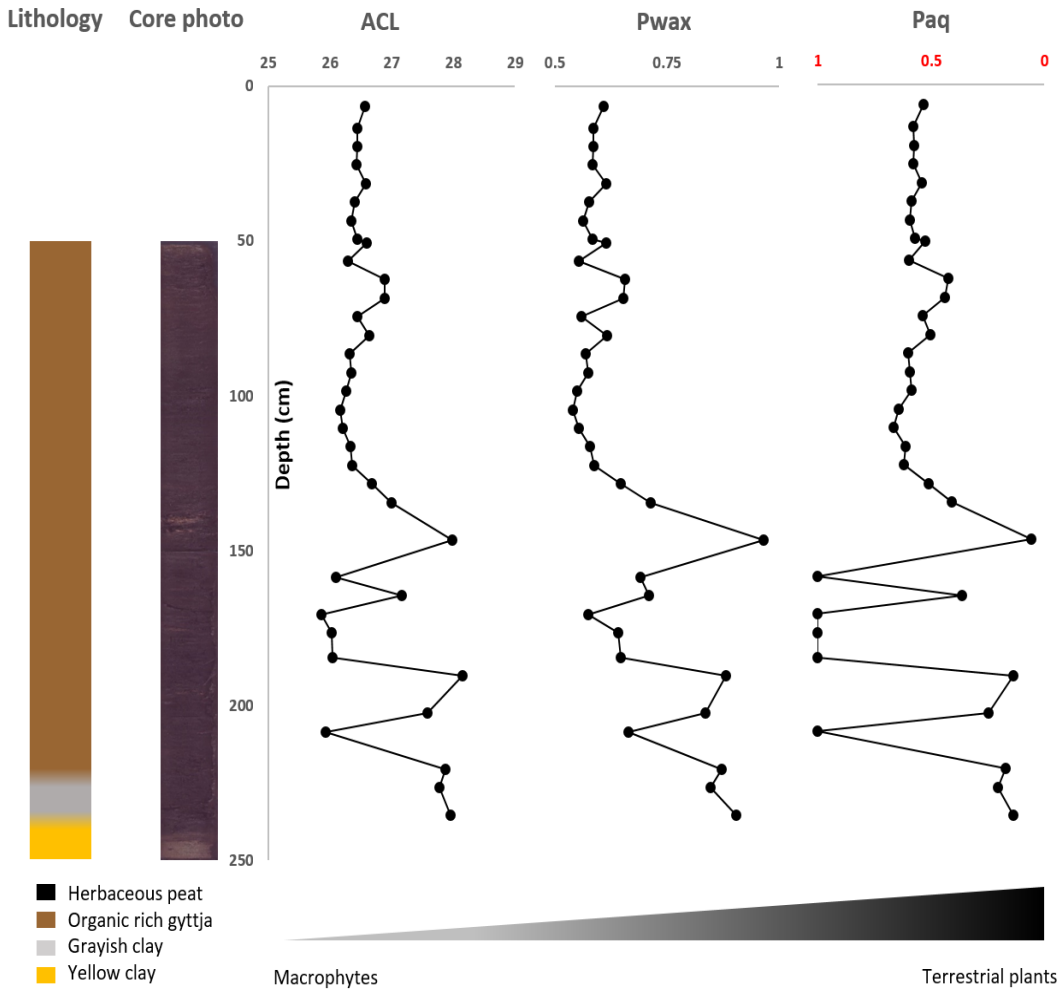

Figure 30. Core lithology, core photo, ACL values (left), P_{wax} values (middle), and P_{aq} values (right) of SXMP_1. Note that P_{aq} is plotted with a reverse scale.

As for SXMP_land 1B, the results are shown in Figure 31, with ACL, P_{wax}, and P_{aq} from left to right. Land 1B shows relatively stable values in the lower part and

doi:10.6342/NTU202304291

fluctuating values in the upper part. The average ACL for SXMP_land 1B is 29.3. The ACL and gradually rises from 400 cm to 312 cm, then slowly declines from 312 cm to 262 cm, reaching its lowest value of 28.6. Subsequently, the measurements become more variable towards the upper part, reaching a peak value of 30.6 at 172 cm. While SXMP_1 showed a positive correlation between ACL and P_{wax}, SXMP_land 1B lacks such clear pattern. The Pwax values in the lower part from 400 cm to 200 cm range between 0.8 and 1, showing no significant deviations. From 200 cm to 142 cm, the values steadily decrease from 0.93 to 0.4. Above 142 cm the measurements continue to fluctuate, ranging from 0.4 to 0.81. Although the trend between P_{wax} and ACL is less pronounced than in SXMP_1, a general agreement between the two proxies can still be discerned. P_{aq} exhibits a strong negative correlation with P_{wax}. Similarly, P_{aq} shows a negative correlation with ACL, though not as pronounced as with P_{wax}. The average P_{aq} value is approximately 0.3, with stable low values from 400 cm to 200 cm, ranging between 0.27 and 0.06. From 200 cm to 142 cm, the values steadily rise to 0.7, followed by a continuous fluctuation from 0.7 to 0.2.

doi:10.6342/NTU202304291

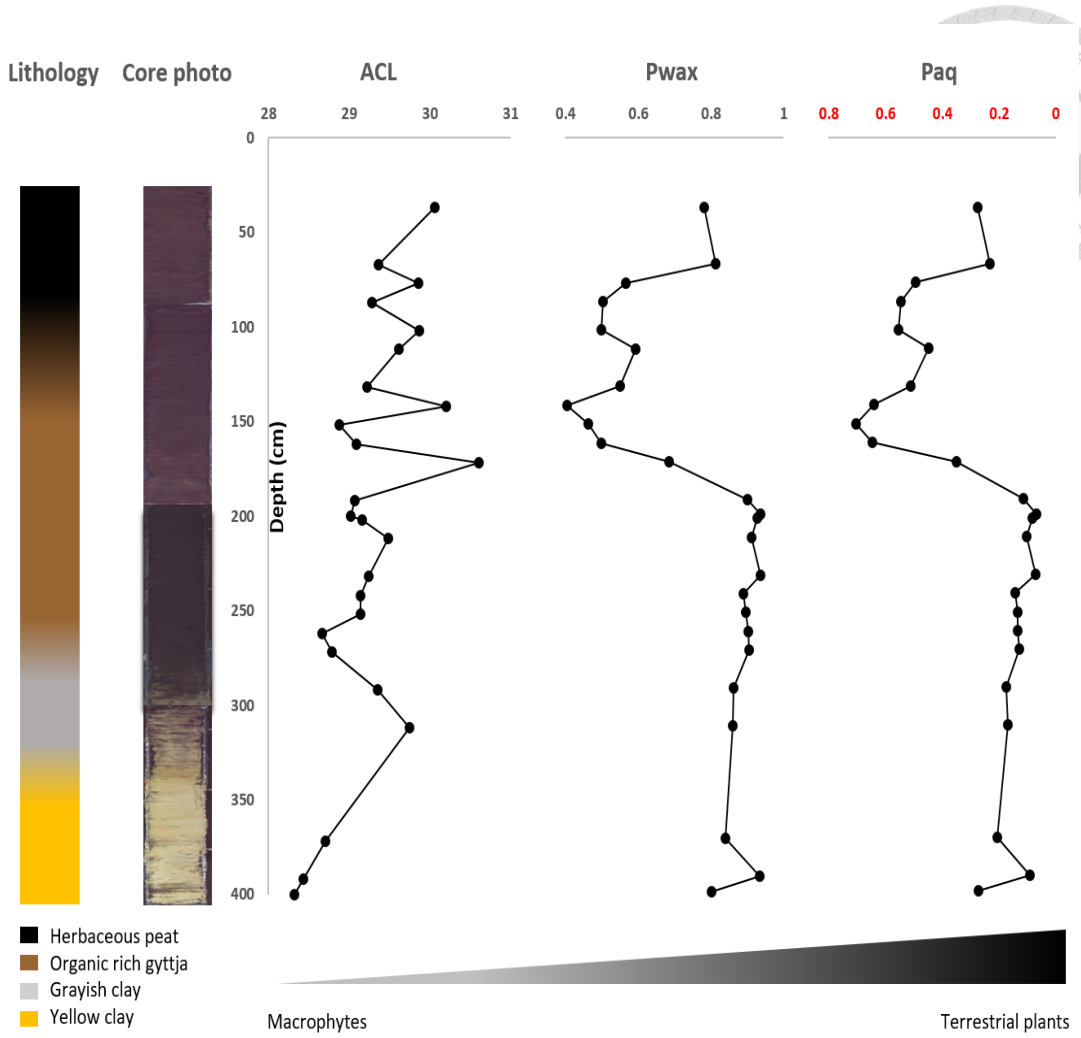

Figure 31. Core lithology, core photo, ACL values (left), P_{wax} values (middle), and P_{aq} values (right) of core SXMP_land 1b. Note that P_{aq} is plotted with a reverse scale.

doi:10.6342/NTU202304291

Chapter 5 Discussion

Chapter 5-1 Origin and formation of Sanxingmei Pond

5-1-1 Determining the lake formation mechanism through the process of exclusion.

According to Hutchinson's classification of major lake types in 1957, this study seeks to eliminate improbable origins by examining relevant evidence. To begin, we exclude the meteorite lake hypothesis. According to the Central Weather Bureau statistics, there is no recorded history of meteorite impact on Taiwan's main island until the end of 2022, and no evidence of high-temperature impact records found in the rocks surrounding the lake. The possibility of anthropogenic lake formation is dismissed as the lake predates any human activities in the Taiping Mountains. The organic lake classification is dismissed, as these small lakes typically emerge in basins connected to beaver dams, coral formations, or vegetation-induced barriers, all of which have not been observed in the study area. Shoreline lake formation is easily dismissed due to the geographical location of the lake itself. Aeolian lake formation is also ruled out. Sanxingmei Pond is in the forest zone, lacking the spacious and arid conditions commonly associated with aeolian lake development (Stauch, 2015). The

doi:10.6342/NTU202304291

absence of significant rivers flowing through the study area, with only a minor stream as input, negates the possibility of fluvial lake formation. Solution lake formation is discarded, given that the lithology of the study area was characterized by insoluble metamorphic bedrock. Glacial lake formation is invalidated due to the absence of glacier traces, erratics, or other indications of glacial activity in the vicinity. Volcanic lake formation is excluded based on the lack of volcanic activity or influence in the Taipingshan area. Lastly, the tectonic lake hypothesis is discounted, considering the size of such lakes, typically generated through geological processes such as tilting, folding, or faulting (Carroll & Bohacs, 1999). Only the Cueifong Lake Fault is located 500 meters to the southeast and does not affect Sanxingmei Pond. After eliminating these ten potential origins, the remaining viable explanation is that of a landslide lake scenario.

5-1-2 Evidence of Sanxingmei Pond being a landslide lake

Based on the conclusions drawn from the above process of elimination, we hypothesize that Sanxingmei Pond falls within the category of landslide lakes. By combining the regional geological map with field surveys conducted across the entire wetland area, we identified the base of the slope encircling the horizontal terrain. This feature is believed to align with the outline of the paleolake (Figure 32).

doi:10.6342/NTU202304291

Furthermore, the slate pieces within the dry, yellowish clay suggest that these materials were deposited in an exposed river valley through subaerial processes before the lake's formation. This observation provides evidence that the basin initially existed as a river valley. Overlying these yellow clays lies a layer of gray clay, characterized by features indicative of lacustrine deposition. Consequently, the boundary between the yellow and gray clay layers corresponds to the event of damming and subsequent lake formation. Therefore, we expect this boundary to be isochronous throughout the entire basin, differing from the upper boundaries which show time-transgressive features.

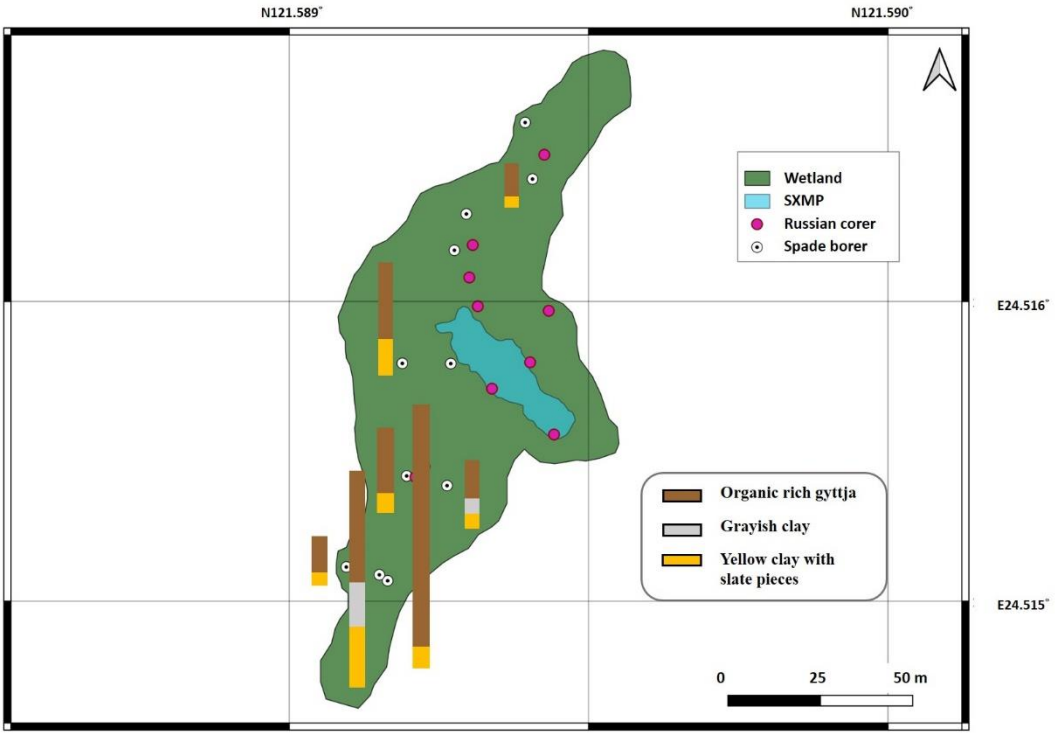

Figure 32. The distribution diagram of seven spade borer cores reveals slate pieces in the yellow clay at the bottom of the sediment cores.

doi:10.6342/NTU202304291

5-2 Alternative explanations for the age reversals in radiocarbon ages

Among the radiocarbon dated cores, the most puzzling results were obtained from core SXMP_land 1b. By the principle of superposition, older ages are expected to occur at greater depths. However, several age reversals were observed, whereby ages from lower sediment layers appeared chronologically younger than those from upper layers. Here, we consider possible origins of the age reversals.

Figure 33 displays two contrasting age models. We present a Bayesian age model on the left-hand side with outliers effectively removed. In contrast, the right-hand side, retains indications of reversals, possibly implying overturned strata. The Bayesian age model for SXMP_land 1b is from the OxCal program, after outlier removal. This produces a profile that is consistent with the superposition principle, as noted above in Chapters 4-4. It is worth highlighting that at depths of 357.5 cm, 276.5 cm to 267.5 cm, and 220.5 cm, distinctive peaks emerge in the right-hand side of the linear age model, where indications of age reversals persist, suggest the presence of overturned strata.

doi:10.6342/NTU202304291

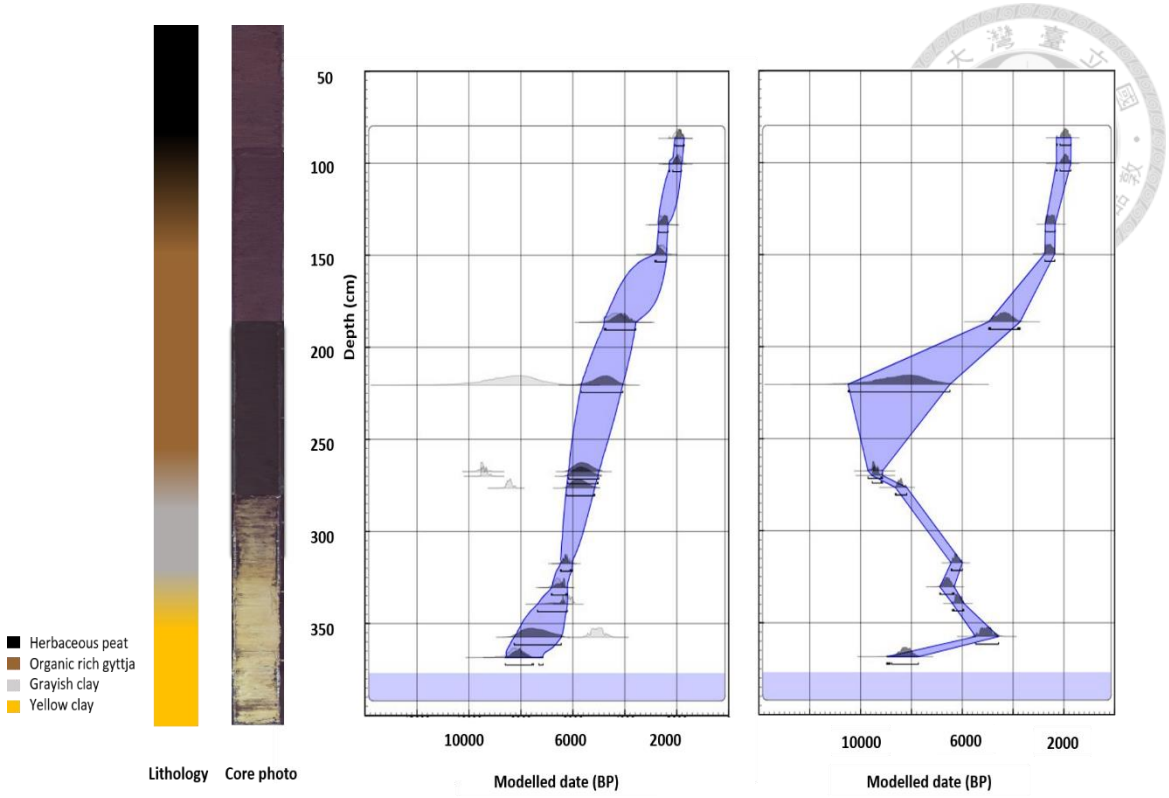

Figure 33. Lithology, core photo, and a Bayesian model. The panel on the right side displays the age model that has undergone linear interpolation. (The core sample is preserved starting from a depth of 35 cm.)

Below, we have summarized several potential processes contributing to the age reversals:

1. Floating Island: Floating islands, also known as floating carpets or mats, as defined by Austin (1979), encompass deposits from floating vegetation and various types of greenery, either living or dead. This phenomenon can be observed in locations like the Shuanglianpi Wetland in Yilan, Taiwan, where floating islands are prone to movement due to strong winds. When a floating

doi:10.6342/NTU202304291

island is moved by strong winds, it may become folded or even overturned, leading to an inversion of the sediment sequence, resulting in age reversals. Figure 34 depicts a floating island, as illustrated by Gleason et al. (1980), alongside an aerial photograph taken at Shuanglianpi.

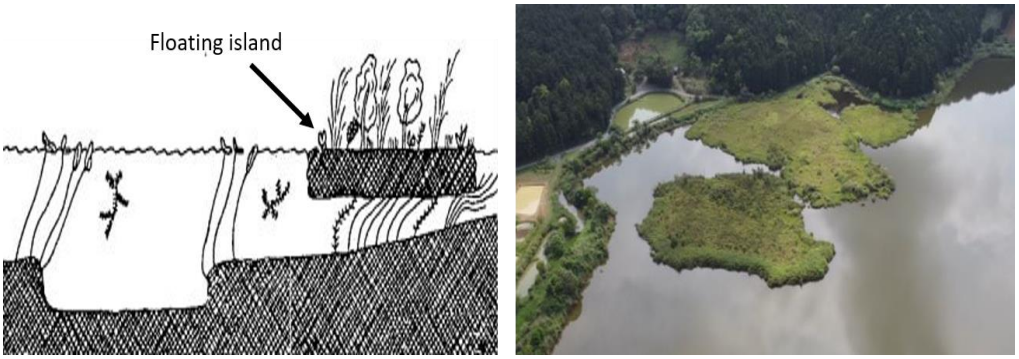

Figure 34. A schematic representation of a floating island (left) and an actual case photograph (right).

2. Contamination during coring: Two possible scenarios can occur. A) Downward displacement of young particles during coring can result in anomalously young ages. B) Upward movement of older particles during core extraction can lead to anomalously old ages. Additionally, improper cleaning of instruments during the selection of radiocarbon dating samples might lead to contamination and biased results. This factor is considered more plausible an age reversal occurs at the boundary between sediments.

doi:10.6342/NTU202304291

3. Landslide: Rapid sediment deposition from a landslide could lead to anomalous radiocarbon dating results. The lack of terrain conducive to landslides in the SXMP wetland area diminishes the likelihood of this factor.

Based on these possibilities, we conclude that the most likely cause of age reversal is the inversion of floating islands. However, the limited density of samples in this study preclude a definitive assessment. Additional radiocarbon dates with representatives from various depths is necessary to validate our hypotheses. Meanwhile, during the core sampling and the selection of dating samples, it is essential to reduce errors caused by human factors. A parallel core can also be drilled nearby to test the correlation between age reversals. Table 7 presents different reasons for age reversals and arguments supporting and opposing each theory.

doi:10.6342/NTU202304291

Table 7. Summary of the arguments for and against the different scenarios explaining the age reversal.

	Supporting arguments	Opposing arguments
Floating island	1. An example present in Shuanglianpi, northeastern Taiwan. 2. Its substantial dimensions could in theory engender extensive age reversals.	The TOC and biomarker analyses did not reveal any instances of reversed trends indicative of age reversal.
Contamination during coring	Contamination during the process of core drilling and sample retrieval is virtually unavoidable.	Repeatedly dating the uncertain time frame indicates that it is likely not a result of any errors or artifacts.
Landslide	Widespread collapses have the potential to result in age reversals spanning substantial intervals.	1. None of the analyses or experiments identified any landslide occurrences within the stratigraphy. 2. The affected area features relatively smaller elevation differences, making it less prone to large-scale landslide events.

doi:10.6342/NTU202304291

5-3 Lake succession

5-3-1 Investigation by drilling results

As discussed in Chapter 5-1, we found eight spade borer cores with slate pieces indicating the initial depth of the lake basin. These eight samples provide insight into the nature of the initial basin floor in the wetland area. It is observed that cores from the outer edge of the wetland are shorter in contrast to those from the inner region. This implies that the initial shape of the basin was approximately v-shaped, similar to a river valley.

The process of lake succession can be divided into three distinct stages: open pond, closed fen stage, and forested wooded swamp. We can observe that the boundary between yellow-gray clay and gyttja is consistently found in all cores, and its age becomes progressively younger as it approaches the remaining open water. Figures 5-1, 5-2, and 5-3 shows SXMP_Platform 3, SXMP_1, and SXMP_land 1b, respectively.

First, we analyzed the open pond area represented by SXMP_Platform 3 (Figure 35). The core was subjected only to AMS-^{14}C dating and XRF analysis. The sedimentation rate is the highest among the three cores, likely attributable to the nearby creek facilitating a continuous influx of sediments.

doi:10.6342/NTU202304291

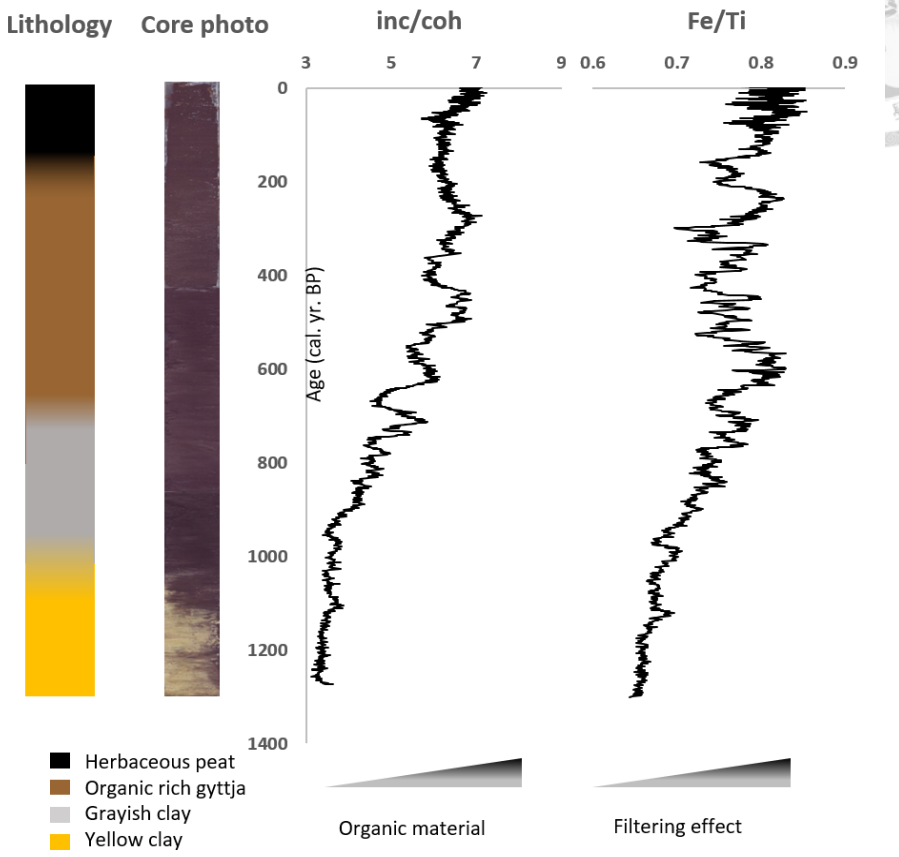

Figure 35. Core lithology, core photo, and XRF results plotted against age for SXMP_Platform 3.

Core SMXP_1 (Figure 36), situated at the present-day lake margin, transitioning to the closed fen stage, exhibits the following characteristics:

1. The boundary between clay and gyttja is approximately dated to 9125 years ago, indicating the beginning of considerable deposition of organic materials derived from various plants and animals. This delineates a shift from oligotrophic open lake to eutrophic pond.

doi:10.6342/NTU202304291

2. We observed a significant increase in Total Organic Carbon (TOC) content between 11,000 and 5,500 years ago, indicating pronounced organic enrichment during the closed fen stage. Subsequently, TOC content has decreased from 5,500 years ago to the present, with the last 3,000 years showing remarkable stability, suggesting a consistent source of sedimentary material in recent times. The C/N ratio follows a trend similar to TOC, with higher values in older sediments, indicating the relative importance of vascular plants (high C/N) versus algae (low C/N). Biomarker results reinforce these patterns, with a notable peak between 4,200 and 3,500 years ago, signifying increased terrestrial plant-derived organic matter input during this period. These findings illustrate the evolving sedimentary dynamics and sources of organic matter over time in the closed fen stage.

Significant fluctuations in sedimentary conditions in SXMP_1 can be attributed to its proximity to the lake edge, leading to alternating periods of open pond and closed fen stage environments. The extent of these variations is particularly pronounced before 3500 years.

doi:10.6342/NTU202304291

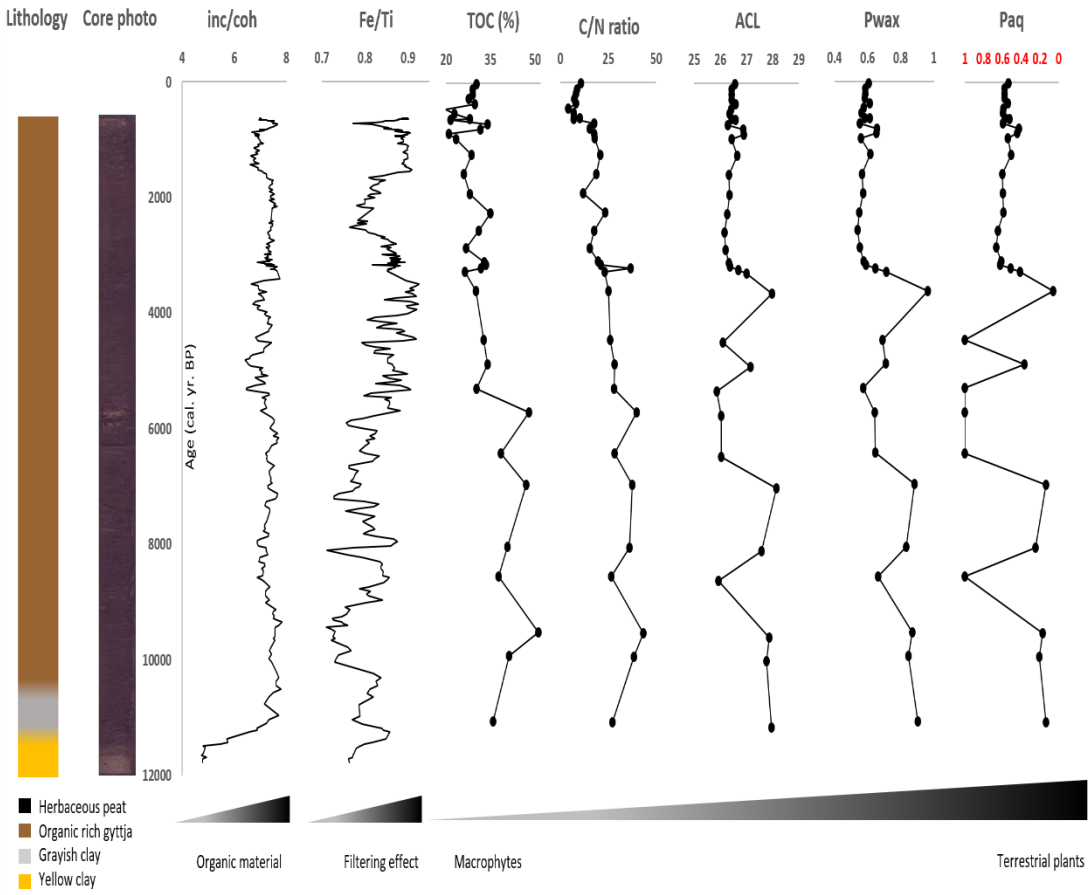

Figure 36. Core lithology, core photo, XRF results, and geochemical sediment parameters (TOC and Biomarkers) plotted against age for SXMP_1. (No XRF measurement data is available for the top 50 cm of SXMP_1.)

Last, SXMP_land 1b represented a forested wooded swamp (Figure 37).

1. The boundary between clay and gyttja is dated to approximately 5930 years ago, signifying a shift in the sedimentary environment with the influx of plant and organic matter around that period.

doi:10.6342/NTU202304291

2. We noted the distinct trends in the XRF data from the SXMP_land 1b core, located in the forested wooded swamp, compared to the other two cores. Approximately 6,000 years ago, a significant increase in XRF values for inc/coh and Fe/Ti indicates a notable shift in sedimentary conditions. This shift is concurrent with changes in TOC and C/N ratios, suggesting alterations in organic matter deposition. Additionally, biomarker values remain relatively stable in the core's lower segment, while a pronounced increase in ACL values occurred between 4,200 and 3,500 years ago, with contrasting trends in Pwax and Paq. These findings highlight distinctive sedimentary dynamics and variations in organic matter sources within the forested wooded swamp during specific time intervals.

doi:10.6342/NTU202304291

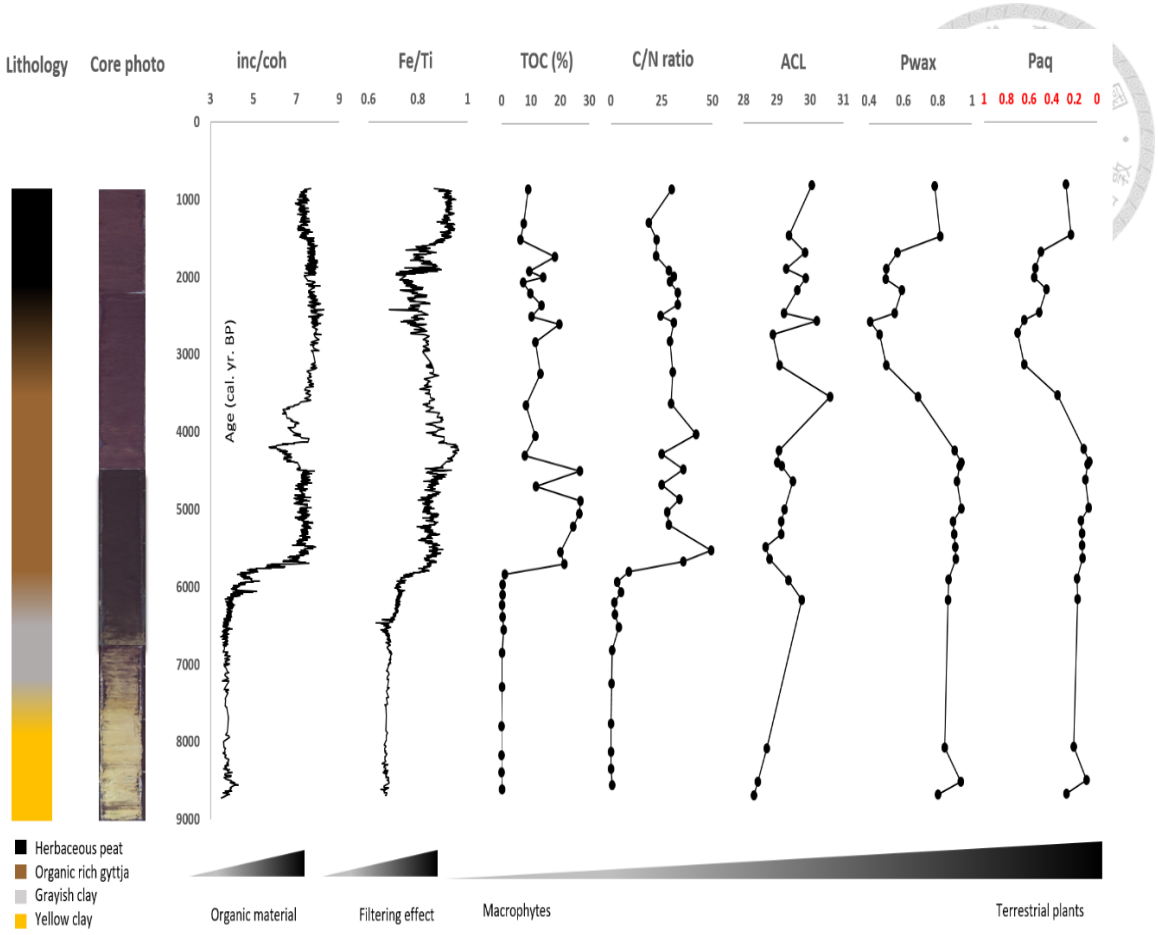

Figure 37. Core lithology, core photo, XRF results, and geochemical sediment parameters (TOC and Biomarkers) plotted against age for SXMP_land 1b.

By synthesizing the various factors influencing different proxies across the three cores, we have gained an understanding of the evolution of Sanxingmei Pond. By examining core descriptions representing different environmental contexts, we have also discerned that the boundary between yellow-gray clay and gyttja varies with distance. Specifically, the boundary tends to be older when located farther from the lake's center and progressively younger as it approaches the current position of the

doi:10.6342/NTU202304291

pond. This suggests a gradual reduction in the lake's size, with fens and wetland environments progressively encroaching upon the open water area.

5-3-2 Lake Succession Dynamics in Sanxingmei Pond

Initially, the Sanxingmei Pond likely looked similar to the present Sanxing Pond (Figure 38). Sanxing Pond is approximately 150 meters northwest of Sanxingmei Pond, with an elevation about 100 meters higher than Sanxingmei Pond. The total surface area of Sanxing Pond is approximately 10,000 square meters, which is comparable to the catchment area of Sanxingmei Pond, measuring 13,000 square meters. Using bathymetric sonar measurements, we estimated maximum depth of approximately 5 to 6 meters, forming a V-shaped basin that broadly aligns with the surrounding geomorphological features. Based on these characteristics, we classify the Sanxing Pond as still belonging to the "open pond" stage in the lake succession process.

doi:10.6342/NTU202304291

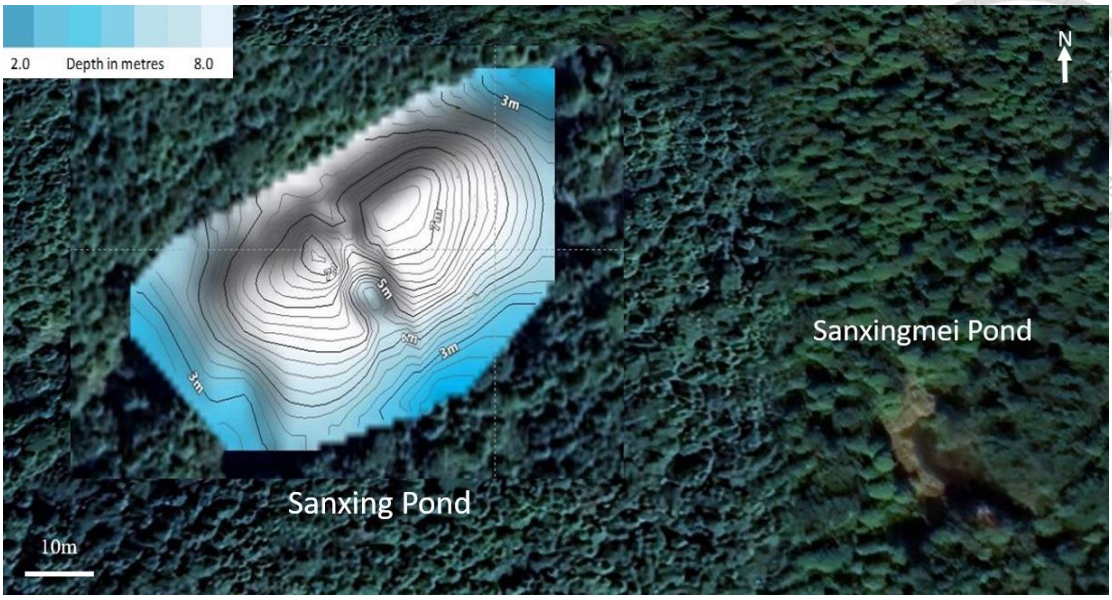

Figure 38. Satellite imagery of Sanxing Pond and Sanxingmei Pond.

Roughly 12,000 years ago, the formation of a closed lake occurred due to a nearby landslide blocking the outflow. Around 9,000 years ago, the boundary between clay and gyttja within SXMP_1 revealed an influx of plant and debris into the lake, indicating shifts in the sedimentary environment. From 12,000 to 6,000 years ago, higher organic carbon deposition characterized the closed fen-stage areas. Around 5,930 years ago, another influx of plant and animal-derived debris marked a shift in sedimentary conditions. A peak in input from terrestrial plants emerged between 4,200 and 3,500 years ago. Since 3,500 years ago, there have been minimal fluctuations in the sedimentary environment.

Nonetheless, according to the sedimentation rate, the lake's overall contraction rate has shown a gradual increase. This progression is graphically illustrated in Figure

doi:10.6342/NTU202304291

39. The process of lake succession involves three distinct stages: the open pond, closed fen stage, and forested wooded swamp. Initially, the open pond phase experienced continuous sediment influx, leading to sediment compaction and the gradual accumulation of sediments along the lake's original margins. This sediment accumulation promoted the growth of macrophytes within the lake, effectively intercepting and hindering further sediment input. Consequently, the lake's size diminished progressively, hastening the transformation of the entire pond into a forested wooded swamp.

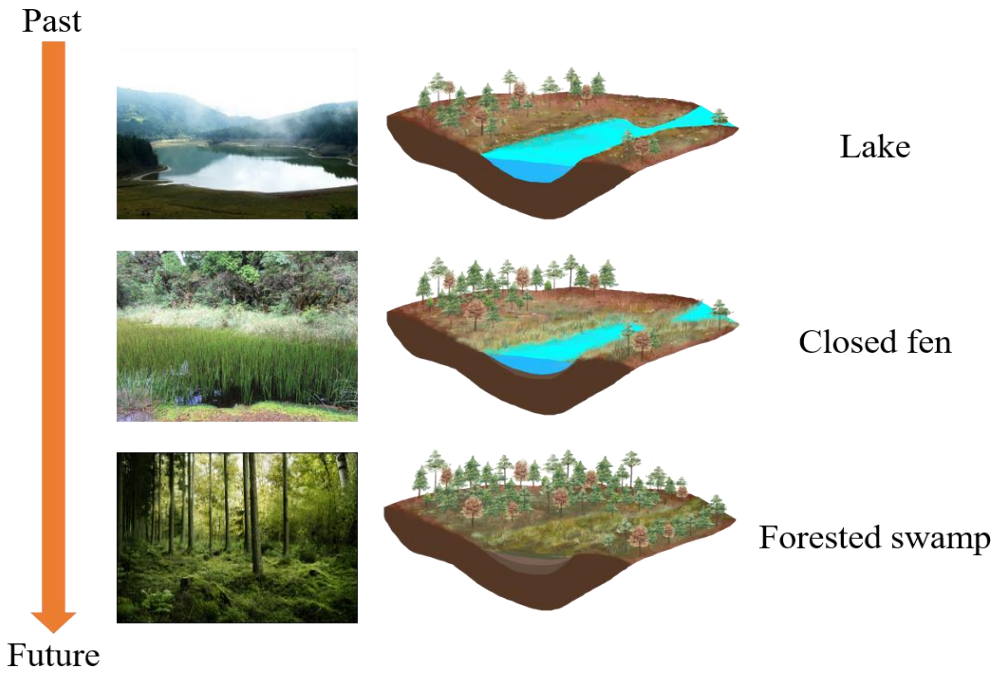

Figure 39.The lake succession model. (Modified by Wong, adapted from Rydin et al., 2013)

doi:10.6342/NTU202304291

Chapter 6 Conclusions

Based on the analysis of multiple sediment cores from Sanxingmei Pond, northeastern Taiwan, the following conclusions can be made:

1. In the high mountainous regions of northeastern Taiwan, the investigation into the origins of small alpine lakes led us to eliminate various potential causes, complemented by the utilization of spade borers for paleo wetland core sampling. In this context, the most plausible explanation for lake formation is the obstruction of valleys by landslides, resulting in the formation of lakes.
2. Age reversal phenomena encountered during standard dating experiments within confined lake basin can have several possible explanations, including floating islands, coring contamination, and landslide events. After analyzing core sample data and comparing dating results across different cores, we conclude that the age reversal observed in the SXMP_land 1b core is most likely attributed to the presence of a floating island that overturned, perhaps in response to typhoons.
3. Evidence derived from the discovery of slate pieces as initial basin infill and applying multiple geochemical analyses to core samples obtained with a Russian corer provides insights into the succession of Sanxingmei Pond. This succession

doi:10.6342/NTU202304291

comprises three distinct stages: an open pond stage, a closed fen stage, and a transition into a forested wooded swamp. Furthermore, varying dating results indicate that sedimentation rates in the later stages accelerate as the pond's surface area diminishes, hastening the overall disappearance of the pond.

Understanding the lake formation, the causes of age reversal in the radiocarbon dating results, as well as lake succession are crucial when interpreting paleolimnological archives.

doi:10.6342/NTU202304291

References

Aaby, B., & Digerfeldt, G. (1986). Sampling techniques for lakes and bogs. *Handbook of holocene palaeoecology and palaeohydrology*, *181*, 194.

Appleby, P. (2001). Chronostratigraphic techniques in recent sediments. *Tracking environmental change using lake sediments: basin analysis, coring, and chronological techniques*, 171-203.

Austin, S. A. (1979). *Depositional environment of the Kentucky No. 12 coal Bed (Middle Pennsylvanian) of Western Kentucky, with special reference to the origin of coal lithotypes*. The Pennsylvania State University.

Bakri, F., Sumardani, D., & Muliyati, D. (2021). Radioactive decay model based on augmented reality. Journal of Physics: Conference Series,

Beckhoff, B., Kanngießer, B., Langhoff, N., Wedell, R., & Wolff, H. (2007). *Handbook of practical X-ray fluorescence analysis*. Springer Science & Business Media.

Blake, A., Chadwick, B., White, P., & Jones, C. (2007). Assessing Sediment Transport at Navy Facilities (User's Guide).

Boak, E. H., & Turner, I. L. (2005). Shoreline definition and detection: a review. *Journal of coastal research*, *21*(4), 688-703.

Bornette, G., Amoros, C., & Lamouroux, N. (1998). Aquatic plant diversity in riverine wetlands: the role of connectivity. *Freshwater biology*, *39*(2), 267-283.

Brock, F., Higham, T., Ditchfield, P., & Ramsey, C. B. (2010). Current pretreatment methods for AMS radiocarbon dating at the Oxford Radiocarbon Accelerator Unit (ORAU). *Radiocarbon*, *52*(1), 103-112.

Burr, G., Jull, A., Gross, M., & Caprioli, R. (2009). Accelerator mass spectrometry for radiocarbon research. *Encyclopedia of mass spectrometry*, *5*, 656-669.

Carrivick, J. L., & Tweed, F. S. (2013). Proglacial lakes: character, behaviour and geological importance. *Quaternary Science Reviews*, *78*, 34-52.

Carroll, A. R., & Bohacs, K. M. (1999). Stratigraphic classification of ancient lakes: Balancing tectonic and climatic controls. *Geology*, *27*(2), 99-102.

Chen, C.-S., & Chen, Y.-L. (2003). The Rainfall Characteristics of Taiwan. *Monthly Weather Review*, *131*, 1323-1341.

Chen, S.-H., Wu, J.-T., Yang, T.-N., Chuang, P.-P., Huang, S.-Y., & Wang, Y.-S. (2009). Late Holocene paleoenvironmental changes in subtropical Taiwan inferred from pollen and diatoms in lake sediments. *Journal of Paleolimnology*, *41*, 315-327.

Cranwell, P. A. (1973). Chain-length distribution of n-alkanes from lake sediments in

doi:10.6342/NTU202304291

relation to post-glacial environmental change. *Freshwater biology*, *3*(3), 259-265.

Croudace, I. W., Rindby, A., & Rothwell, R. G. (2006). ITRAX: description and evaluation of a new multi-function X-ray core scanner. *Geological Society, London, Special Publications*, *267*(1), 51-63.

Crozaz, G., Picciotto, E., & De Breuck, W. (1964). Antarctic snow chronology with Pb210. *Journal of Geophysical Research*, *69*(12), 2597-2604.

Dean, M. C., Le Cabec, A., Van Malderen, S. J., & Garrevoet, J. (2020). Synchrotron X-ray fluorescence imaging of strontium incorporated into the enamel and dentine of wild-shot orangutan canine teeth. *Archives of oral biology*, *119*, 104879.

Dean, W. E. (1981). Carbonate minerals and organic matter in sediments of modern north temperate hard-water lakes.

Dearing, J. (1991). Lake sediment records of erosional processes. Environmental History and Palaeolimnology: Proceedings of the Vth International Symposium on Palaeolimnology, held in Cumbria, UK,

Downing, J. A., Prairie, Y., Cole, J., Duarte, C., Tranvik, L., Striegl, R. G., McDowell, W., Kortelainen, P., Caraco, N., & Melack, J. (2006). The global abundance and size distribution of lakes, ponds, and impoundments. *Limnology and oceanography*, *51*(5), 2388-2397.

Ficken, K. J., Li, B., Swain, D., & Eglinton, G. (2000). An n-alkane proxy for the sedimentary input of submerged/floating freshwater aquatic macrophytes. *Organic Geochemistry*, *31*(7-8), 745-749.

Garcia-Castellanos, D. (2006). Long-term evolution of tectonic lakes: climatic controls on the development of internally drained basins.

Gleason, P. J., Piepgras, D., Stone, P. A., & Stipp, J. (1980). Radiometric evidence for involvement of floating islands in the formation of Florida Everglades tree islands. *Geology*, *8*(4), 195-199.

Godwin, H. (1962). Half-life of radiocarbon. *Nature*, *195*(4845), 984-984.

Goldberg, E. D. (1963). Geochronology with lead-210, radioactive dating, IAEA. *Vienna*, *1*, 21-131.

Hatté, C., & Jull, A. (2015). 14C in Plant Macrofossils. In.

Havens, K. E., Sharfstein, B., Brady, M. A., East, T. L., Harwell, M. C., Maki, R. P., & Rodusky, A. J. (2004). Recovery of submerged plants from high water stress in a large subtropical lake in Florida, USA. *Aquatic Botany*, *78*(1), 67-82.

Hirose, K. (2012). 2011 Fukushima Dai-ichi nuclear power plant accident: summary of regional radioactive deposition monitoring results. *Journal of environmental radioactivity*, *111*, 13-17.

doi:10.6342/NTU202304291

Holgerson, M. A., & Raymond, P. A. (2016). Large contribution to inland water CO2 and CH4 emissions from very small ponds. *Nature Geoscience*, *9*(3), 222-226. https://doi.org/10.1038/ngeo2654

Hsu, S.-T. (2015). Modern sediment dispersal paths and mechanisms off southwestern Taiwan.

Huang, Y., Shuman, B., Wang, Y., & Webb, T. (2004). Hydrogen isotope ratios of individual lipids in lake sediments as novel tracers of climatic and environmental change: a surface sediment test. *Journal of Paleolimnology*, *31*, 363-375.

Huh, C.-A., & Su, C.-C. (1999). Sedimentation dynamics in the East China Sea elucidated from 210Pb, 137Cs and 239,240 Pu. *Marine Geology*, *160*(1-2), 183-196.

Hutchinson, G. E., & Edmondson, Y. H. (1957). *A treatise on limnology / George Evelyn Hutchinson*. John Wiley.

Jansen, J., Van der Gaast, S., Koster, B., & Vaars, A. (1998). CORTEX, a shipboard XRF-scanner for element analyses in split sediment cores. *Marine Geology*, *151*(1-4), 143-153.

Kalnicky, D. J., & Singhvi, R. (2001). Field portable XRF analysis of environmental samples. *Journal of hazardous materials*, *83*(1-2), 93-122.

Kershaw, A. P. (1997). A modification of the Troels-Smith system of sediment description and portrayal. *Quaternary Australasia*, *15*(2), 63-68.

Klaminder, J., Appleby, P., Crook, P., & Renberg, I. (2012). Post-deposition diffusion of 137Cs in lake sediment: Implications for radiocaesium dating. *Sedimentology*, *59*(7), 2259-2267.

Korponai, J., Braun, M., Buczkó, K., Gyulai, I., Forró, L., Nédli, J., & Papp, I. (2010). Transition from shallow lake to a wetland: a multi-proxy case study in Zalavári Pond, Lake Balaton, Hungary. *Hydrobiologia*, *641*, 225-244.

Löwemark, L., Chen, H.-F., Yang, T.-N., Kylander, M., Yu, E.-F., Hsu, Y.-W., Lee, T.-Q., Song, S.-R., & Jarvis, S. (2011). Normalizing XRF-scanner data: a cautionary note on the interpretation of high-resolution records from organic-rich lakes. *Journal of Asian Earth Sciences*, *40*(6), 1250-1256.

Löwemark, L., Bloemsma, M., Croudace, I., Daly, J. S., Edwards, R. J., Francus, P., Galloway, J. M., Gregory, B. R., Huang, J.-J. S., & Jones, A. F. (2019). Practical guidelines and recent advances in the Itrax XRF core-scanning procedure. *Quaternary International*, *514*, 16-29.

Łachacz, A., Nitkiewicz, M., & Pisarek, W. (2009). Soil conditions and vegetation on gyttia lands in the Masurian Lakeland. *Contemporary Problems of Management and Environmental Protection Wetlands–Their Functions and*

doi:10.6342/NTU202304291

Protection, *2*, 61-94.

Lan, J., Wang, T., Chawchai, S., Cheng, P., Yu, K., Yan, D., Wang, Y., Zang, J., Liu, Y., & Tan, L. (2020). Time marker of 137Cs fallout maximum in lake sediments of Northwest China. *Quaternary Science Reviews*, *241*, 106413.

Lau, K.-M., & Li, M.-T. (1984). The monsoon of East Asia and its global associations—A survey. *Bulletin of the American Meteorological Society*, *65*(2), 114-125.

Leng, M. J., & Marshall, J. D. (2004). Palaeoclimate interpretation of stable isotope data from lake sediment archives. *Quaternary Science Reviews*, *23*(7-8), 811-831.

Li, Y.-H., Chen, C., & Hung, J.-J. (1997). Aquatic chemistry of lakes and reservoirs in Taiwan. *TAO*, *8*(4), 405.

Libby, W. F., & Johnson, F. (1955). *Radiocarbon dating* (Vol. 2). University of Chicago Press Chicago.

Liew, P.-M., Huang, S.-Y., & Kuo, C.-M. (2006). Pollen stratigraphy, vegetation and environment of the last glacial and Holocene—a record from Toushe Basin, central Taiwan. *Quaternary International*, *147*(1), 16-33.

Liew, P.-M., Wu, M.-H., Lee, C.-Y., Chang, C.-L., & Lee, T.-Q. (2014). Recent 4000 years of climatic trends based on pollen records from lakes and a bog in Taiwan. *Quaternary International*, *349*, 105-112.

Lin, C. (2009). Conferring the Composition and Distribution of Vegetation Diversity in Taiwan. *Master's Thesis*.

Lin, S.-F. (2004). *Environmental and Climatic Changes in Ilan Plain over the Recent 4200 Years as Revealed by Pollen Data and their Relationship to Prehistory colonization (in Chinese)* (Publication Number 2004 年) 國立臺灣大學]. AiritiLibrary.

Lin, S.-F., Huang, T.-C., Liew, P.-M., & Chen, S.-H. (2007). A palynological study of environmental changes and their implication for prehistoric settlement in the Ilan Plain, northeastern Taiwan. *Vegetation history and archaeobotany*, *16*, 127-138.

Lin, T.-W., Kaboth-Bahr, S., Bahr, A., Yamoah, K. A., Su, C.-C., Wang, L.-C., Wang, P.-L., & Löwemark, L. (2023). Disentangling the impact of anthropogenic and natural processes on the environment in a subtropical subalpine lake catchment in northeastern Taiwan over the past 150 years. *Science of The Total Environment*, *866*, 161300.

Liritzis, I., & Zacharias, N. (2011). Portable XRF of archaeological artifacts: current research, potentials and limitations. *X-ray fluorescence spectrometry (XRF) in geoarchaeology*, 109-142.

doi:10.6342/NTU202304291

Lou, J.-Y., Chen, C.-T. A., & Wann, J.-K. (1997). Paleoclimatological records of the Great Ghost Lake in Taiwan. *Science in China Series D: Earth Sciences*, *40*, 284-292.

McNichol, A. P., Jull, A. J. T., & Burr, G. S. (2001). Converting AMS Data to Radiocarbon Values: Considerations and Conventions. *Radiocarbon*, *43*(2A), 313-320. https://doi.org/10.1017/s0033822200038169

Merkt, J. (1971). Reliable counting of annually laminated layers of lake sediments by means of long-sized thin sections. *Arch. Hydrobiol*, *69*, 145-154.

Pennington, W., Tutin, T., Cambray, R., & Fisher, E. (1973). Observations on lake sediments using fallout 137Cs as a tracer. *Nature*, *242*(5396), 324-326.

Pitkänen, A., & Lukasiuk, K. (2011). Mechanisms of epileptogenesis and potential treatment targets. *The Lancet Neurology*, *10*(2), 173-186.

Poynter, J., & Eglinton, G. (1990). 14. Molecular composition of three sediments from hole 717c: The Bengal fan. Proceedings of the Ocean Drilling Program: Scientific results,

Poynter, J., Farrimond, P., Robinson, N., & Eglinton, G. (1989). Aeolian-derived higher plant lipids in the marine sedimentary record: Links with palaeoclimate. *Paleoclimatology and paleometeorology: modern and past patterns of global atmospheric transport*, 435-462.

Ramage, C. S. (1971). Monsoon meteorology. *(No Title)*.

Ramsey, C. B. (2009). Bayesian analysis of radiocarbon dates. *Radiocarbon*, *51*(1), 337-360.

Richardson, D. C., Holgerson, M. A., Farragher, M. J., Hoffman, K. K., King, K. B., Alfonso, M. B., Andersen, M. R., Cheruveil, K. S., Coleman, K. A., & Farruggia, M. J. (2022). A functional definition to distinguish ponds from lakes and wetlands. *Scientific reports*, *12*(1), 10472.

Ritchie, J. C., & McHenry, J. R. (1990). Application of radioactive fallout cesium-137 for measuring soil erosion and sediment accumulation rates and patterns: A review. *Journal of environmental quality*, *19*(2), 215-233.

Rothwell, R. G., Hoogakker, B., Thomson, J., Croudace, I. W., & Frenz, M. (2006). Turbidite emplacement on the southern Balearic Abyssal Plain (western Mediterranean Sea) during Marine Isotope Stages 1–3: an application of ITRAX XRF scanning of sediment cores to lithostratigraphic analysis. *Geological Society, London, Special Publications*, *267*(1), 79-98.

Rouwet, D., Tassi, F., Mora-Amador, R., Sandri, L., & Chiarini, V. (2014). Past, present and future of volcanic lake monitoring. *Journal of Volcanology and Geothermal Research*, *272*, 78-97.

Schleiss, A. J., Franca, M. J., Juez, C., & De Cesare, G. (2016). Reservoir

doi:10.6342/NTU202304291

sedimentation. *Journal of Hydraulic Research*, *54*(6), 595-614.

Schlolaut, G., Brauer, A., Marshall, M. H., Nakagawa, T., Staff, R. A., Ramsey, C. B., Lamb, H. F., Bryant, C. L., Naumann, R., & Dulski, P. (2014). Event layers in the Japanese Lake Suigetsu 'SG06'sediment core: description, interpretation and climatic implications. *Quaternary Science Reviews*, *83*, 157-170.

Schnitchen, C., Charman, D. J., Magyari, E., Braun, M., Grigorszky, I., Tóthmérész, B., Molnár, M., & Szántó, Z. (2006). Reconstructing hydrological variability from testate amoebae analysis in Carpathian peatlands. *Journal of Paleolimnology*, *36*, 1-17.

Schnurrenberger, D., Russell, J., & Kelts, K. (2003). Classification of lacustrine sediments based on sedimentary components. *Journal of Paleolimnology*, *29*, 141-154.

Schumacher, B. A. (2002). *Methods for the determination of total organic carbon (TOC) in soils and sediments*. US Environmental Protection Agency, Office of Research and Development ….

Scott, A. G. (2003). SUB-FOSSIL SPIDERS FROM HOLOCENE PEAT CORES. *The Journal of Arachnology*. https://doi.org/10.1636/0161-8202

Selvaraj, K., Wei, K.-Y., Liu, K.-K., & Kao, S.-J. (2012). Late Holocene monsoon climate of northeastern Taiwan inferred from elemental (C, N) and isotopic (δ13C, δ15N) data in lake sediments. *Quaternary Science Reviews*, *37*, 48-60.

Simoneit, B. R., Sheng, G., Chen, X., Fu, J., Zhang, J., & Xu, Y. (1991). Molecular marker study of extractable organic matter in aerosols from urban areas of China. *Atmospheric Environment. Part A. General Topics*, *25*(10), 2111-2129.

Stauch, G. (2015). Geomorphological and palaeoclimate dynamics recorded by the formation of aeolian archives on the Tibetan Plateau. *Earth-Science Reviews*, *150*, 393-408.

Stenström, K., Skog, G., Georgiadou, E., Genberg, J., & Mellström, A. (2011). A guide to radiocarbon units and calculations.

Thomson, J., Croudace, I., & Rothwell, R. (2006). A geochemical application of the ITRAX scanner to a sediment core containing eastern Mediterranean sapropel units. *Geological Society, London, Special Publications*, *267*(1), 65-77.

Tjallingii, R., Röhl, U., Kölling, M., & Bickert, T. (2007). Influence of the water content on X-ray fluorescence core-scanning measurements in soft marine sediments. *Geochemistry, Geophysics, Geosystems*, *8*(2).

Troels-Smith, J. (1955). *Characterization of unconsolidated sediments*. Reitzels Forlag.

Verpoorter, C., Kutser, T., Seekell, D. A., & Tranvik, L. J. (2014). A global inventory of lakes based on high-resolution satellite imagery. *Geophysical Research*

doi:10.6342/NTU202304291

Letters, *41*(18), 6396-6402. https://doi.org/10.1002/2014gl060641

Wang, L.-C., Lee, T.-Q., Chen, S.-H., & Wu, J.-T. (2010). Diatoms in Liyu lake, eastern Taiwan. *Taiwania*, *55*(3), 228-242.

Williams, P., Whitfield, M., Biggs, J., Bray, S., Fox, G., Nicolet, P., & Sear, D. (2004). Comparative biodiversity of rivers, streams, ditches and ponds in an agricultural landscape in Southern England. *Biological conservation*, *115*(2), 329-341.

Woolway, R. I., Kraemer, B. M., Lenters, J. D., Merchant, C. J., O'Reilly, C. M., & Sharma, S. (2020). Global lake responses to climate change. *Nature Reviews Earth & Environment*, *1*(8), 388-403. https://doi.org/10.1038/s43017-020-0067-5

Wu, J.-T., Chuang, P.-P., Wu, L.-Z., & Chen, C.-T. A. (1997). Diatoms as indicators of environmental changes: a case study in Great Ghost Lake. *Proceedings of the National Science Council, Republic of China. Part B, Life Sciences*, *21*(3), 112-119.

Wu, J.-T., & Wang, Y.-F. (2009). Diatoms of the Mystery Lake, Taiwan (III). *Taiwania*, *54*(3), 231-240.

Xing, Y., Xie, P., Yang, H., Ni, L., Wang, Y., & Rong, K. (2005). Methane and carbon dioxide fluxes from a shallow hypereutrophic subtropical Lake in China. *Atmospheric Environment*, *39*(30), 5532-5540.

Yamoah, K. A., Callac, N., Chi Fru, E., Wohlfarth, B., Wiech, A., Chabangborn, A., & Smittenberg, R. H. (2016). A 150-year record of phytoplankton community succession controlled by hydroclimatic variability in a tropical lake. *Biogeosciences*, *13*(13), 3971-3980.

Zheng, Y., Zhou, W., Meyers, P. A., & Xie, S. (2007). Lipid biomarkers in the Zoigê-Hongyuan peat deposit: Indicators of Holocene climate changes in West China. *Organic Geochemistry*, *38*(11), 1927-1940.

doi:10.6342/NTU202304291